



A maximum likelihood approach to diffeomorphic speckle tracking for 3D strain estimation in echocardiography



Ariel H. Curiale^{a,*}, Gonzalo Vegas-Sánchez-Ferrero^{b,c}, Johan G. Bosch^d,
Santiago Aja-Fernández^a

^a Laboratorio de Procesado de Imagen (LPI), E.T.S. Ingenieros de Telecomunicación, Universidad de Valladolid, Valladolid, Spain

^b Applied Chest Imaging Laboratory (ACIL), Brigham and Womens Hospital, Harvard Medical School, 1249 Boylston St., Boston, MA 02115, USA

^c Biomedical Image Technologies Laboratory (BIT), ETSI Telecomunicación, Universidad Politécnica de Madrid, and CIBER-BBN, Avenida Complutense 30, Madrid, 28040, Spain

^d Thoraxcenter Biomedical Engineering, Erasmus University Medical Center, Rotterdam, The Netherlands

ARTICLE INFO

Article history:

Received 21 November 2014

Revised 11 February 2015

Accepted 4 May 2015

Available online 23 May 2015

Keywords:

Strain and motion estimation

Speckle tracking

Maximum likelihood

Mixture model

Diffeomorphic registration

ABSTRACT

The strain and strain-rate measures are commonly used for the analysis and assessment of regional myocardial function. In echocardiography (EC), the strain analysis became possible using Tissue Doppler Imaging (TDI). Unfortunately, this modality shows an important limitation: the angle between the myocardial movement and the ultrasound beam should be small to provide reliable measures. This constraint makes it difficult to provide strain measures of the entire myocardium. Alternative non-Doppler techniques such as Speckle Tracking (ST) can provide strain measures without angle constraints. However, the spatial resolution and the noisy appearance of speckle still make the strain estimation a challenging task in EC. Several maximum likelihood approaches have been proposed to statistically characterize the behavior of speckle, which results in a better performance of speckle tracking. However, those models do not consider common transformations to achieve the final B-mode image (e.g. interpolation). This paper proposes a new maximum likelihood approach for speckle tracking which effectively characterizes speckle of the final B-mode image. Its formulation provides a diffeomorphic scheme than can be efficiently optimized with a second-order method. The novelty of the method is threefold: First, the statistical characterization of speckle generalizes conventional speckle models (Rayleigh, Nakagami and Gamma) to a more versatile model for real data. Second, the formulation includes local correlation to increase the efficiency of frame-to-frame speckle tracking. Third, a probabilistic myocardial tissue characterization is used to automatically identify more reliable myocardial motions. The accuracy and agreement assessment was evaluated on a set of 16 synthetic image sequences for three different scenarios: normal, acute ischemia and acute dyssynchrony. The proposed method was compared to six speckle tracking methods. Results revealed that the proposed method is the most accurate method to measure the motion and strain with an average median motion error of 0.42 mm and a median strain error of $2.0 \pm 0.9\%$, $2.1 \pm 1.3\%$ and $7.1 \pm 4.9\%$ for circumferential, longitudinal and radial strain respectively. It also showed its capability to identify abnormal segments with reduced cardiac function and timing differences for the dyssynchrony cases. These results indicate that the proposed diffeomorphic speckle tracking method provides robust and accurate motion and strain estimation.

© 2015 Elsevier B.V. All rights reserved.

1. Introduction

Regional heart function plays an important role in the treatment and diagnosis of different cardiac pathologies such as mitral regurgitation (Messas et al., 2001), ischemia (Voigt et al., 2003; Yeon et al., 2001) and dyssynchrony (Suffoletto et al., 2006). The early detection

* Corresponding author.

E-mail address: ariel@lpi.tel.uva.es, curiale@gmail.com (A.H. Curiale).

and treatment of regional abnormalities could predict and prevent global functional changes and it has shown important clinical implications (Abraham et al., 2007). In particular, the strain (tissue deformation) and strain rate (speed at which deformation occurs) are commonly used to assess the regional myocardial function (Dandel et al., 2009). For example, Messas et al. (2001) showed that papillary muscle (PM) can decrease the mitral regurgitation by reducing leaflets tethering. In their work, they made use of the strain rate to assess the longitudinal PM contraction non-invasively, without PM instrumentation. Voigt et al. (2003) studied the regional strain and strain

rate to differentiate ischemic and nonischemic regional ischemia during dobutamine stress echocardiography. Likewise, Suffoletto et al. (2006) showed that strain can be used to quantify dyssynchrony and to predict immediate and long-term response to cardiac resynchronization therapy.

In echocardiography, the strain and strain rate can be measured by using Doppler-based techniques, *Tissue Doppler Imaging* (TDI), or non-Doppler techniques known as *Strain Imaging* (SI) and *Speckle Tracking* (ST). Similar to the conventional blood velocity Doppler techniques, Tissue Doppler comes in a number of varieties: Pulsed wave spectral Doppler measures myocardial velocities at a single position, 2D Color Doppler within an image region of interest. However, all Doppler techniques can only assess the velocity component along the direction of the ultrasound beam. Thus, all these techniques suffer from angle dependence in the assessment of tissue velocities. This is one of the explanations why this technique has not become standard in daily Praxis (Dandel et al., 2009). In contrast, ST and SI techniques can estimate angle independent tissue velocities in the entire image, since they are not based on the Doppler principles (Amundsen et al., 2006).

Ultrasound (US) data in EC is generated by the reflection of transmitted coherent ultrasound waves at fixed frequencies. The result of the interaction between those waves and different types of tissues give rise to the interference phenomenon known as *speckle*. This interference pattern, though it is textured with noisy visual aspect, remains unaltered under the same acquisition conditions, i.e. the same transducer aperture, pulse length and transducer angle. This behavior exhibits an inherent relationship with the tissue structure that can be tracked to estimate the motion and deformation of the heart (Burkhardt, 1978). The methods that analyze motion by tracking the intensity or the interference patterns produced by speckle along the temporal sequences of a US acquisition in B-mode are known as *Speckle Tracking* methods. These methods have proved to be useful tools to obtain quantitative and qualitative information regarding myocardial deformation, motion and function assessment (Helle-Valle et al., 2005; Notomi et al., 2005). In the particular case when the motion is analyzed by tracking the speckle from the RF signal, these methods are referred as *Strain Imaging* (Konofagou and Ophir, 1998; Lopata et al., 2011; O'Donnell et al., 1994).

In the US community, a particular methodology for motion estimation, known as block-matching, has received special attention due to its simplicity and performance (Bohs et al., 2000; Cohen and Dinstein, 2002; Nesser et al., 2009; Strintzis and Kokkinidis, 1997; Suffoletto et al., 2006). However, this methodology is confined to estimate the motion in a particular search block, which results in a disadvantage for big complex motions. Recently, several authors proposed new speckle tracking methods by using more flexible approaches to overcome this limitation. Most of them use a variational optical flow approach (Alessandrini et al., 2013; Somphone et al., 2013; Tautz et al., 2013) or a Free-Form Deformation approach (FFD) (Curiale et al., 2013; Heyde et al., 2013; Myronenko et al., 2009; Piella et al., 2013).

An interesting contribution to motion estimation in US with block-matching was proposed by Strintzis and Kokkinidis (1997), where a maximum likelihood (ML) methodology was used to provide a suitable metric for US images based on a multiplicative Rayleigh characterization. Cohen and Dinstein (2002) extended the proposal to include the relationship between the multiplicative Rayleigh characterizations of consecutive frames, which resulted in a better performance for speckle tracking. However, these approaches present the inherent problems of the original block-matching: they cannot follow the complex deformation due to its block-wise analysis. Besides, some effects of processing during the acquisition of US data cause a deviation from the Rayleigh assumption that reduces its suitability for the description of speckle statistics.

These limitations were avoided by the proposals of Myronenko et al. (2009) and Curiale et al. (2013), which adapted different ML approaches to FFD schemes based on b-splines and more realistic statistical models. Specifically, Myronenko et al. (2009) considered that the backscattered signal is received in the probe as a result of the integration in some area of the detector. Thus, the Rayleigh speckle model is no longer valid. Instead, they proposed a bivariate Nakagami distribution with a temporal correlation between frames. In contrast, Curiale et al. (2013) proposed a Gamma model to characterize the integration of different Rayleigh distributed signals, which has shown better fitting behavior than the Nakagami model (Vegas-Sánchez-Ferrero et al., 2010).

The main advantage of Myronenko's in contrast to Cohen's and Curiale's models is that it exploits the high correlation between two consecutive frames. However, the Nakagami approach can be substantially improved with more suitable statistical models that successfully generalize Nakagami and Gamma distributions, such as the Generalized Gamma model (Vegas-Sánchez-Ferrero et al., 2012). Besides, Myronenko's shows an important limitation since it assumes a homogeneous correlation between consecutive frames, which is clearly a non-realistic assumption since the speckle in the blood pool would not show the same correlation as other regions with a more stable speckle response. As a result of this, the correlation between frames should be carefully estimated considering a spatially variant behavior. The aim of our proposal is to successfully generalize the conventional speckle models (Rayleigh (Cohen and Dinstein, 2002; Strintzis and Kokkinidis, 1997), Nakagami (Myronenko et al., 2009) and Gamma (Curiale et al., 2013)) with the inclusion of an adaptive temporal correlation between consecutive frames. The statistical characterization is also used to automatically identify reliable myocardial motions. This is an important contribution that provides more accurate estimates of the strain and strain rate measures. In this way, the main advantages of a suitable and versatile statistical model and the temporal coherence are considered throughout the speckle tracking process. Additionally, to provide a smooth and invertible (diffeomorphic) motion field, the proposed method leads to a formulation which can be efficiently implemented in a diffeomorphic demons approach instead of the FFD technique used by Myronenko et al. (2009) and Curiale et al. (2013).

In conclusion, this paper proposes an accurate diffeomorphic speckle tracking methodology for 3D strain estimation in final EC B-mode images, which presents three main contributions: First, we provide a speckle model and a formulation that generalizes the previous speckle models (Rayleigh, Nakagami and Gamma) into a more versatile one, better adaptable to real data (Vegas-Sánchez-Ferrero et al., 2012). The formulation derived perspective allows to provide two different similarity measures to deal with data in different steps of the acquisition (prior and post log-compression). Furthermore, the speckle model allows to define a diffeomorphic demons-based approach with an efficient second-order minimization scheme. Second, we introduce a formulation which considers an adaptive temporal correlation to improve the speckle tracking. To the best of our knowledge, this is the first time that the correlation is adaptively estimated. Third, a probabilistic myocardial tissue characterization is used to automatically identify more reliable myocardial motions. In particular, this contribution reduces the negative effect of unreliable myocardial motions such as those introduced by the blood pool or shadowing artifacts by means of a probabilistic regularization according to the reliability of motions.

The proposed methodology was evaluated in the *Straus* dataset proposed by De Craene et al. (2013), which provides a realistic cardiac geometry and a complex motion for different ischemia and dyssynchrony types, and normal cases with different signal to noise ratios. Besides, it provides results of five different and relevant speckle tracking algorithms, leading to reproducible studies.

2. Background

This section briefly describes the methodologies under comparison in this paper. In particular we will describe the classical diffeomorphic demons method proposed by Vercauteren et al. (2009), which leads to derive the diffeomorphic formulation of the proposed method used for comparison.

2.1. Demons registration

Inspired by the optical flow equation (Beauchemin and Barron, 1995), Thirion (1998) proposed to consider non-rigid registration as a diffusion process. In his work, he introduced the idea of demons that push according to the local characteristics of the images in a similar way Maxwell did for solving the Gibbs paradox. In each iteration, the demons forces are introducing a displacement update into the motion field. In general, this algorithm alternates between computation of forces and a regularization step. Vercauteren et al. (2009) showed that the demons algorithms could be seen as an optimization procedure for a global energy on the entire space of displacement fields. Also, they showed that the demons algorithm could be adapted to provide a non-parametric diffeomorphic transformation. The difference with respect to the original approach amounts to how the Jacobian is computed and how the instant update is considered. In the classical demons, the update is a dense displacement field, whereas in the diffeomorphic demons the update is considered as a speed vector field. Moreover, when the images are aligned with the optimal spatial transformation, the fixed image and the warped images as well as their gradient should be very close to each other. In that case, the symmetric forces could be linked to the efficient second-order minimization framework, which is one of the most useful contributions proposed by Vercauteren et al. (2009) and it will be used in our proposal.

2.2. Speckle tracking methods

Philips: Somphone et al. (2013) propose a fast implementation of a demons-like algorithm. In their proposal, the similarity measure is the sum of squared intensity difference (SSD) and the motion estimation is confined to the myocardial tissue by using a manual segmentation and normalized convolution (Knutsson and Westin, 1993). Furthermore, the optimization is performed in a variational approach by using a gradient descent within a multiresolution refinement approach.

Creatis: Alessandrini et al. (2013) propose a monogenic phase motion estimation algorithm based on a variational optical flow. This technique uses the monogenic phase of the image for extracting image features instead of using the image intensities. The motion is estimated by solving the optical flow equation locally on a sliding spatial window. Also, several B-spline windows are defined at different scale and the motion transformation is assumed to be locally affine. Finally, the motion is iteratively refined by using a coarse-to-fine multiresolution scheme.

KU Leuven: Heyde et al. (2013) propose to use an anatomical FFD model for motion estimation. The motion transformation is modeled by using B-splines and the basis functions are locally oriented along the radial, longitudinal and circumferential direction of the endocardium. They use the SSD as similarity measure and a bound-constrained optimizer (Byrd et al., 1995). The motion estimation was then projected back into the cartesian coordinates to compute the strain.

UPF: Piella et al. (2013) propose a diffeomorphic FFD algorithm to handle the temporal dimension. In their proposal, the similarity measure takes into account sequential and fixed-reference terms. The sequential term makes use of a Rayleigh speckle model between

consecutive images (Cohen and Dinstein, 2002), while the fixed-reference term uses the SSD between each image and the first image in the sequence. The fixed-reference term provides a drift correction in the whole motion estimation. Similarly to the KU Leuven approach, this method use B-splines for modeling the motion transformation and a large-scale bound constrained (LBFGSB) algorithm for optimizing the temporal similarity measure.

Mevis: Tautz et al. (2013) propose another monogenic phase motion estimation algorithm. In particular, his proposal is based on the Morphons algorithm originally proposed by Knutsson and Andersson (2005). In this technique, the quadrature filter provides a certainty map which is used to iteratively refine the motion estimation. Instead of processing the whole 3D volume at once, the displacements are computed for 2D slices, and then, the final 3D motion is created by combining the 2D contributions.

3. Proposed method

The proposed method is intentionally designed to measure the strain and strain rate by identifying reliable myocardial motions and by taking into account the US images acquisition and formation. With this aim, a flexible and general statistical model is needed in order to deal with the effect of the signal integration in the detector and the temporal correlation between consecutive frames. According to the results shown in Vegas-Sanchez-Ferrero et al. (2012), the Generalized Gamma offers a versatile model that effectively generalizes the Gamma or Nakagami speckle model. The inclusion of the temporal correlation between consecutive frames can be included within the statistical model by means of the relationship of a Bivariate Generalized Gamma, whose joint distribution presents a correlation factor that must be estimated. This fact substantially entangles the parameter estimation of the statistical model, however, this difficulty can be efficiently avoided, as we explain in further sections, by the application of a Generalized Gamma mixture model (Vegas-Sanchez-Ferrero et al., 2012) jointly with a local estimation of the correlation coefficient. The use of mixture models not only leads to an efficient estimation of the temporal correlation, but also provides important information to identify more reliable myocardial motions, improving the performance of the method on measuring the strain and strain rate.

3.1. Diffeomorphic maximum likelihood motion estimation

In US dynamics, ML has been successfully used to estimate the motion between two images acquired under the same acquisition conditions at consecutive time instances (Cohen and Dinstein, 2002; Curiale et al., 2013; Myronenko et al., 2009). This can be formalized by considering X_t and X_{t-1} as two motion related frames at time t and $t-1$. Then, the transition of pixels between time t and $t-1$ is described by the transformation $s: \mathbf{x} \rightarrow \mathbf{x} + \mathbf{s}(\mathbf{x})$ where $\mathbf{x} \in X_t$ and $\mathbf{x} + \mathbf{s}(\mathbf{x}) \in X_{t-1}$. Now, let $\Omega_x = \{\mathbf{x} \in X_t | s^{-1}(\mathbf{x}) \in X_{t-1}\}$ the overlap region between images, $I_t = \{I_t(\mathbf{x})\}_{\mathbf{x} \in \Omega_x}$ be the intensity image at time t and $I_{t-1} \circ s = \{I_{t-1} \circ s(\mathbf{x})\}_{\mathbf{x} \in \Omega_x}$ be the intensity image at time $t-1$. Then, the ML estimation of s , \hat{s}_{ML} , is obtained by maximizing the following likelihood (Strintzis and Kokkinidis, 1997):

$$\begin{aligned} \hat{s}_{ML} &= \arg \max_s p(I_{t-1} | I_t, s) \\ &= \arg \max_s \prod_{\mathbf{x} \in \Omega_x} p(I_{t-1} \circ s(\mathbf{x}) | I_t(\mathbf{x}), s), \end{aligned} \quad (1)$$

which is equivalent to minimizing the normalized negative log-likelihood $\Lambda(s)$:

$$\begin{aligned} \Lambda(s) &= \frac{1}{N} \sum_{\mathbf{x} \in \Omega_x} -\log(p(I_{t-1} \circ s(\mathbf{x}) | I_t(\mathbf{x}), s)) \\ &= \frac{1}{N} \sum_{\mathbf{x} \in \Omega_x} \varphi_{\mathbf{x}}(I_t, I_{t-1} \circ s), \end{aligned} \quad (2)$$

where N is the overlap number of voxels. Note that all the conditional probabilities are supposed to be independent and identically distributed (IID).

A common model used for characterizing US images is to consider the speckle as signal-dependent pattern. Consequently, the US image could be modeled as $I(\mathbf{x}) = a(\mathbf{x}) \eta_0(\mathbf{x})$, where $\eta_0(\mathbf{x})$ is a multiplicative pattern with probability density function (PDF), $p_\eta(\cdot)$; and $a(\mathbf{x})$ is the true image intensity (Kotropoulos et al., 1994). Assuming that the true value of the acquisition, $a(\mathbf{x})$, remains unaltered after the deformation, the following equality holds (Cohen and Dinstein, 2002):

$$I_{t-1} \circ s(\mathbf{x}) = I_t(\mathbf{x}) \eta \quad (3)$$

where $\eta = I_{t-1} \circ s(\mathbf{x}) / I_t(\mathbf{x}) = \eta_1 / \eta_2$ is the ratio between two random variables. Moreover, the likelihood of $I_{t-1} \circ s(\mathbf{x})$ can be calculated as a simple transformation of IID random variables, η , given $I_t(\mathbf{x})$ and the displacement field $s(\mathbf{x})$:

$$\begin{aligned} p(I_{t-1} \circ s(\mathbf{x}) | I_t(\mathbf{x}), s) &= \frac{1}{I_t(\mathbf{x})} p_\eta(\eta) \\ &= \frac{1}{I_t(\mathbf{x})} p_\eta\left(\frac{I_{t-1} \circ s(\mathbf{x})}{I_t(\mathbf{x})}\right) \end{aligned} \quad (4)$$

Similarly, taking the natural logarithm out of both sides of Eq. (3) the underlying model is derived as follow:

$$\hat{I}_{t-1} \circ s(\mathbf{x}) = \hat{I}_t(\mathbf{x}) + \hat{\eta} \quad (5)$$

where $\hat{I}_t = \ln(I_t)$ and $\hat{\eta} = \ln(\eta)$. In this case, the conditional probability density function is given by:

$$\begin{aligned} p(I_{t-1} \circ s(\mathbf{x}) | I_t(\mathbf{x}), s) &= \eta p_\eta(\eta) \\ &= \frac{I_{t-1} \circ s(\mathbf{x})}{I_t(\mathbf{x})} p_\eta\left(\frac{I_{t-1} \circ s(\mathbf{x})}{I_t(\mathbf{x})}\right) \end{aligned} \quad (6)$$

Eqs. (4) and (6) can be calculated using the well-known Change of Variables Theorem for random variables.

So far the formulation has been derived for random variables which follow generic probability distributions. In order to provide a versatile model for speckle the Generalized Gamma (GG) distribution introduced in Stacy (1962) is adopted due to its suitability for modeling real EC B-mode images (Vegas-Sanchez-Ferrero et al., 2012). This distribution is especially attractive since it generalizes in a natural way the conventional Gamma model and other commonly used distributions such as Rayleigh, Nakagami and Weibull.

The temporal correlation is included in the statistical model by introducing a bivariate GG speckle model with equal shape and scale parameters which leads to a ratio between consecutive frames, $\eta = \eta_1 / \eta_2 = I_{t-1} \circ s(\mathbf{x}) / I_t(\mathbf{x})$, where the joint distribution of η_1 and η_2 is the bivariate GG distribution proposed in Piboongunton et al. (2005), whose marginal distributions follow the conventional GG distribution proposed in Stacy (1962). With this probabilistic model, the ratio η is distributed as follows (Bithas et al., 2007):

$$\begin{aligned} p_\eta(\eta) &= \frac{\beta 2^{2m}}{\sqrt{\pi} (1-\rho)^{-m}} \frac{\Gamma(m+0.5)}{\Gamma(m)} \\ &\quad \cdot \frac{\eta^{2\beta m-1}}{(\eta^{2\beta} + 1)^{2m}} \left(1 - \frac{4\rho\eta^{2\beta}}{(\eta^{2\beta} + 1)^2}\right)^{-\frac{2m+1}{2}} \end{aligned} \quad (7)$$

where m and β are shape parameters (Bithas et al., 2007) and ρ is the correlation between different time frames I_{t-1} and I_t defined as:

$$\rho = \frac{\text{cov}(I_{t-1}^2, I_t^2)}{\sqrt{\text{Var}(I_{t-1}^2)\text{Var}(I_t^2)}} \quad (8)$$

One important advantage of this statistical model is that the formulation derived for the ratio of correlated GG distributions can be easily adapted to the different steps of the acquisition process of the image. Specifically, it can be accommodated to the image intensities

before and after the log-compression during the acquisition process. Thus, depending on the step of the formulation we want to model, two different similarity measures can be defined. In what follows, φ_{GGS} will refer to the similarity measure, without log-compression, whereas φ_{GGCS} stands for the measure of log-compressed images.

The first similarity measure, φ_{GGS} , and its gradient can be derived directly from the ratio of two GG random variables substituting the Eq. (7) into Eq. (4) as follows (the detailed derivation is presented in Appendix A):

$$\begin{aligned} \varphi_{\text{GGS}}^s(\mathbf{x}) &= \log(I_t(\mathbf{x})) - (2\beta m - 1) \log(\eta) - \log(\eta^{2\beta} + 1) \\ &\quad + (m + 0.5) \log((\eta^{2\beta} + 1)^2 - 4\rho\eta^{2\beta}) \\ &\quad - \log(I_{t-1} \circ s(\mathbf{x})) \end{aligned} \quad (9)$$

$$\begin{aligned} \nabla \varphi_{\text{GGS}}^s(\mathbf{x}) &= \frac{2\beta}{I_{t-1} \circ s(\mathbf{x})} \\ &\quad \left[-m + \eta^{2\beta} \left(\frac{2(\eta^{2\beta} + 1) - 4\rho}{(\eta^{2\beta} + 1)^2 - 4\rho\eta^{2\beta}} \right) \right. \\ &\quad \left. \cdot (m + 0.5) - \frac{1}{\eta^{2\beta} + 1} \right] \nabla J(\mathbf{x}) \end{aligned} \quad (10)$$

where $\nabla J(\mathbf{x}) = \frac{1}{2}(\nabla I_t(\mathbf{x}) + \nabla I_{t-1} \circ s(\mathbf{x}))$. This similarity measure takes into account the interpolation done in the scanner to obtain the final B-mode image and the correlation between two consecutive images and it naturally generalizes the similarity measure proposed in Curiale et al. (2013) with the advantage of considering the temporal correlation between frames.

The second similarity measure proposed, φ_{GGCS} , and its gradient can be derived from the ratio of two Generalized Gamma random variables after logarithmic compression (Eq. (6)) and leads to the following formulation (the detailed derivation is explained in Appendix B):

$$\begin{aligned} \varphi_{\text{GGCS}}^s(\mathbf{x}) &= \frac{2m+1}{2} \log(\cosh^2(\hat{\eta}\beta) - \rho) \\ &\quad - \frac{1}{2} \log(\cosh^2(\hat{\eta}\beta)) \end{aligned} \quad (11)$$

$$\begin{aligned} \nabla \varphi_{\text{GGCS}}^s(\mathbf{x}) &= \left(\frac{2m+1}{\cosh^2(\hat{\eta}\beta) - \rho} - \frac{1}{\cosh^2(\hat{\eta}\beta)} \right) \\ &\quad \cdot \beta \cosh(\hat{\eta}\beta) \sinh(\hat{\eta}\beta) \nabla J(\mathbf{x}) \end{aligned} \quad (12)$$

where $\nabla J(\mathbf{x}) = \frac{1}{2}(\nabla I_t(\mathbf{x}) + \nabla I_{t-1} \circ s(\mathbf{x}))$. This similarity measure also provides a natural generalization of the similarity measures proposed in Myronenko et al. (2009) and Cohen and Dinstein (2002), with the advantage of considering the temporal correlation between frames.

After defining the similarity measures, the normalized negative log-likelihood, Λ , defined in Eq. (2) can be minimized by using several methods such as the classical block-matching, as was done in Cohen and Dinstein (2002); gradient descent algorithm, as in Curiale et al. (2013); or even the steepest descent method as in Myronenko et al. (2009). However, instead of using these approaches, the derived formulation allows us to apply an efficient second-order minimization scheme proposed by Vercauteren et al. (2009) for the demons (Thirion, 1998) approach. The rationale for this choice not only relies on the advantages of the second-order optimization, but also with the capability of providing a diffeomorphic registration, which is a desired property when the deformations are considered for further processing such as the calculation of the strain and strain rate measures. Thus, in our proposal, we adapt the original global energy function defined in the diffeomorphic demons algorithm as follows:

$$\begin{aligned} E_{\mathbf{x}}(c, s) &= \frac{1}{2|\Omega_{\mathbf{x}}|} \sum_{\mathbf{x} \in \Omega_{\mathbf{x}}} \left\| \frac{1}{\sigma_i} \varphi_{\mathbf{x}}(I_t, I_{t-1} \circ c) \right\|^2 \\ &\quad + \frac{1}{\sigma_x^2} \text{dist}(s, c)^2 + \frac{1}{\sigma_T^2} \text{Reg}(s) \end{aligned} \quad (13)$$

where σ_i accounts for the noise on the image intensity, σ_x is the spatial uncertainty on the correspondences, σ_T controls the amount of regularization, $\varphi_x(\cdot)$ corresponds to the similarity measure derived from the ML approach to minimize (Eq. 2), c is a non-parametric spatial transformation which is used to decouple the minimization into simple and very efficient two steps (Vercauteren et al., 2009).

The minimization of the regularization step in Eq. (13) is performed by a single convolution when the regularization is quadratic and uniform. Specifically, if $\text{Reg}(s) = \|\nabla s\|^2$, the optimal regularized deformation field is obtained by a convolution of the deformation field with a Gaussian Kernel (Vercauteren et al., 2009). Therefore, in this work we focused on the first part of Eq. (13), by minimizing the following energy function:

$$E_{\mathbf{x}}^{\text{corr}}(c) = \|\varphi_{\mathbf{x}}(I_t, I_{t-1} \circ c)\|^2 + \frac{\sigma_i^2}{\sigma_x^2} \|c - s\|^2 \quad (14)$$

where $\text{dist}(c, s) = \|c - s\|$. This energy function is rewritten in terms of the displacement field, \mathbf{u} , as follows:

$$E_{\mathbf{x}}^{\text{corr}}(\mathbf{u}) = \frac{1}{2|\Omega_x|} \sum_{\mathbf{x} \in \Omega_x} \|\varphi_{\mathbf{x}}(I_t, I_{t-1} \circ s \circ \exp(\mathbf{u}))\|^2 + \frac{\sigma_i^2}{\sigma_x^2} \|\mathbf{u}\|^2 \quad (15)$$

Now, let us assume that the gradient of the similarity measure is known. Then, the following linearization of the similarity measure, $\varphi_{\mathbf{x}}$, can be derived:

$$\varphi_{\mathbf{x}}^s(\mathbf{u}) \approx \varphi_{\mathbf{x}}^s(0) + J_{\varphi}^{\mathbf{x}} \cdot \mathbf{u} \quad (16)$$

where $\varphi_{\mathbf{x}}^s(0) = \varphi_{\mathbf{x}}(I_t, I_{t-1} \circ s)$, $\varphi_{\mathbf{x}}^s(\mathbf{u}) = \varphi_{\mathbf{x}}(I_t, I_{t-1} \circ s \circ \exp(\mathbf{u}))$ and $J_{\varphi}^{\mathbf{x}}$ is the gradient of the similarity function $\varphi_{\mathbf{x}} : \mathbb{R}^n \rightarrow \mathbb{R}$ at $\mathbf{u} = 0$. Then, Eq. (15) can be rewritten as:

$$E_s^{\text{corr}}(\mathbf{u}) \approx \frac{1}{2|\Omega_x|} \sum_{\mathbf{x} \in \Omega_x} \left\| \begin{bmatrix} \varphi_{\mathbf{x}}(I_t, I_{t-1} \circ s) \\ 0 \end{bmatrix} + \begin{bmatrix} J_{\varphi}^{\mathbf{x}} \\ \frac{\sigma_i}{\sigma_x} Id \end{bmatrix} \cdot \mathbf{u} \right\|^2 \quad (17)$$

Solving the normal equation and using the Sherman–Morrison formula (Sherman and Morrison, 1950), in the same way as was used in Vercauteren et al. (2009), the optimal update that minimizes the energy function E_s^{corr} is:

$$\mathbf{u}(\mathbf{x}) = - \frac{\varphi_{\mathbf{x}}(I_t, I_{t-1} \circ s) J_{\varphi}^{\mathbf{x}^t}}{\|J_{\varphi}^{\mathbf{x}}\|^2 + \frac{\sigma_i^2}{\sigma_x^2}} \quad (18)$$

and the maximum step length is controlled by σ_x with $\|\mathbf{u}\| \leq \sigma_x/2$. Note that if we use $\sigma_i = |\varphi_{\mathbf{x}}|$ and $\varphi_{\mathbf{x}} = I_{t-1} \circ s - I_t$, we end up with the expression of the demons forces originally proposed by Thirion (1998) and also note that an efficient second-order minimization is achieved when $J_{\varphi}^{\mathbf{x}} = \nabla \varphi_{\mathbf{x}}(I_t, I_{t-1} \circ s) (\nabla I_t(x) + \nabla I_{t-1} \circ s(x))$ (see Vercauteren et al. (2009) for more details).

3.2. Parameter estimation and regularization

During the derivation of the registration methodology the parameters of the Generalized Gamma distribution must be estimated. Note that this estimation should consider two important facts: 1) the response of tissues varies spatially; 2) the speckle of displaced locations may present temporal correlation.

The main advantage of the bivariate GG model adopted to describe the nature of speckle is that it allows to naturally split the estimation of different response of tissues and the temporal correlation. This can be achieved because the marginal distributions of the bivariate GG random variable that describes consecutive frames can be marginalized into two GG random variables (Bithas et al., 2007). This way, the responses of each tissue and parameters of the marginalized GG distribution can be analyzed separately in each time frame without considering the temporal correlation, which can be estimated independently.

3.2.1. Estimation of marginal distributions

The different response of tissues can be effectively described by means of the GG mixture model proposed by Vegas-Sanchez-Ferrero et al. (2012). This mixture model can describe the contribution of different GG distributions in the speckle image and, thus, provides a probabilistic information about the nature of each tissue. The mixture model can be calculated by means of the expectation-maximization algorithm (Moon, 1996), which maximizes the log-likelihood function for hidden discrete random variables, $\mathbf{Z} = \{Z_i\}$. Formally speaking, let $\mathbf{X} = \{x_i\}$, $1 \leq i \leq N$ be an identical independent distribution set of samples (pixel intensities) and x_i belongs to the distributions class j when $Z_i = j$. The mixture model considers that these variables result from the contributions of J distributions:

$$p(x_i | \Theta) = \sum_{j=1}^J \pi_j f_X(x_i | \Theta_j) \quad (19)$$

where Θ is a vector of parameters of the mixture model (π_j, Θ_j) and Θ_j are the parameters of the GG distribution function, $\sum_{j=1}^J \pi_j = 1$ and f_X is the PDF of the marginalized GG random variable with the following parametrization¹:

$$f_X(x | \{a_j, \beta_j, m_j\}) = \frac{2\beta_j x^{2\beta_j m_j - 1}}{\Gamma(m_j)} \binom{m_j}{a_j} \exp\left(-\frac{m_j}{a_j} x^{2\beta_j}\right) \quad (20)$$

where $x \geq 0$, $j \in \{1, \dots, J\}$ and a_j is a scale parameter and β_j and m_j are shape parameters. In our case, a set of $J = 2$ classes (blood and tissue) were considered as it was described in Vegas-Sanchez-Ferrero et al. (2012).

Note that the mixture model formulation provides the probability of belonging to each class (blood or tissue), which can be effectively used to identify reliable myocardial motions. The probability of belonging to the j -th class for sample x_i is obtained by means of the Bayes' theorem as:

$$\Upsilon_j(x_i) = P\{Z_i = j | x_i\} = \frac{f_X(x_i | \Theta_j) \pi_j}{p(x_i | \Theta)} \quad (21)$$

In what follows, $\Upsilon = \{\Upsilon_j\}_{j=1..J}$ will denote the set of probabilistic characterizations for all tissue classes.

3.2.2. Regularization of reliable deformations

The probabilistic characterization provides suitable information that can be used to assess the reliability of myocardial motions. In this way, the inherent regularization of the diffeomorphic demons method can be probabilistically weighted to avoid the effect of less reliable deformations in the blood pool that may bias deformations in the myocardial tissue. In order to take advantage of the tissue characterization, the normalized convolution approach proposed by Knutsson and Westin (1993) provides an adequate tool to weight in a different way the contributions of deformations in different tissues. Formally speaking, a deformation field $\mathbf{v}(\mathbf{x})$ can be regularized by considering the probabilistic characterization $\Upsilon_j \in \Upsilon$ as:

$$K \circledast (\mathbf{v}(\mathbf{x}), \Upsilon_j(\mathbf{x})) = \frac{K * (\mathbf{v}(\mathbf{x}) \cdot \Upsilon_j(\mathbf{x}))}{K * \Upsilon_j(\mathbf{x})} \quad (22)$$

where the operator \circledast describes the normalized convolution of the deformation field \mathbf{v} weighted by the probabilistic characterization Υ_j with some kernel K . Note that the most appropriate weights are those that describe the characterization of tissue, since they have higher values in myocardial regions and lower in the blood pool.

¹ Note that the parametrization here used differs from the one followed in Vegas-Sanchez-Ferrero et al. (2012), though they are totally equivalent.

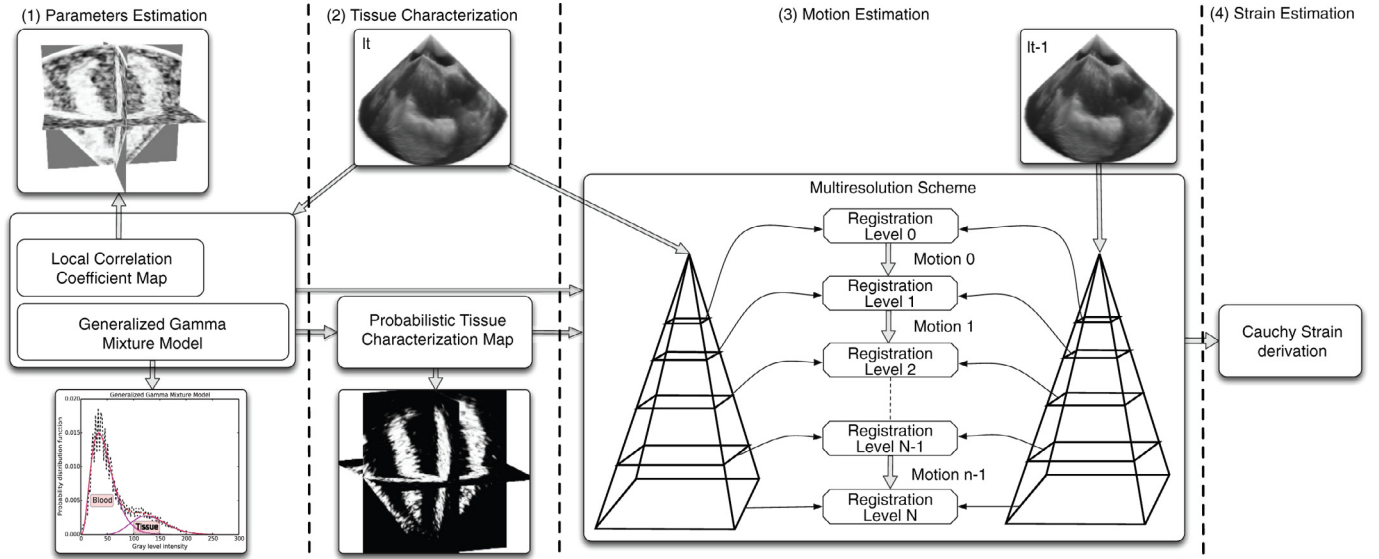


Fig. 1. Work flow of the methodology proposed for motion and strain estimation. The proposed method has four phases: (1) *Parameters Estimation*: a Generalized Gamma mixture model and the local correlation coefficient were used to estimate the parameters involved into the Generalized Gamma speckle model; (2) *Tissue Characterization*: a probabilistic tissue map is calculated for the myocardium; (3) *Motion Estimation*: a multiresolution scheme is used for motion estimation combined with a diffeomorphic demons-based registration; (4) *Strain Estimation*: the strain is derived using the classical Cauchy formulation.

3.2.3. Adaptive temporal correlation

The temporal correlation defined in Eq. (8) for each location of the image is estimated by means of the Local Correlation Coefficient (LCC) defined as follows:

$$\rho(\mathbf{x}) = \text{LCC}(I_{t-1}^2(\mathbf{x}), I_t^2(\mathbf{x})) = \frac{\overline{I_{t-1}^2(\mathbf{x})I_t^2(\mathbf{x})} - \overline{I_{t-1}^2(\mathbf{x})}\overline{I_t^2(\mathbf{x})}}{\sigma_{I_{t-1}^2} \sigma_{I_t^2}} \quad (23)$$

where I_t and I_{t-1} correspond to the image intensities and $\overline{I^2(\mathbf{x})}$ denotes the sample mean value of I^2 in a local neighborhood of \mathbf{x} , which can be computed as the local spatial average using a normalized and symmetric kernel G_η , i.e. $\overline{I^2(\mathbf{x})} = \sum_{\mathbf{k}} G_\theta(\mathbf{x} - \mathbf{k}) I_t^2(\mathbf{k})$. There are multiple choices for the kernel G_θ ; in our case, we consider a normalized Gaussian window with isotropic covariance θ^2 in order to avoid any direction preferences and to give more importance to those values near the location under study.

3.3. Summary and implementation details

Our proposal for motion and strain estimation can be summarized in the following four phases, also described in Fig. 1, where a multiresolution scheme is applied:

1. *Parameters Estimation*: A GG mixture model is used to estimate the parameters of the marginal GG distributions of Eq. (20) involved in the proposed speckle model π_j , $\Theta_j = \{a_j, \beta_j, m_j\}$ for $j = 1, 2$. The correlation between two consecutive images in the cardiac phase is estimated using the local correlation by Eq. (23).
2. *Tissue Characterization*: The parameters estimated in the *Parameters Estimation* phase are used to calculate the probabilistic tissue characterization for the myocardium by means of Eq. (21).
3. *Motion Estimation*: The motion field estimation is achieved by using a ML motion estimation for a bivariate Generalized Gamma speckle model through a diffeomorphic demons registration as follows:
 - (a) *Similarity measures*: The similarity measures derived from a ML approach for a bivariate GG speckle model are calculated by using Eqs. (9) and (10) in the case of non-compressed images or Eqs. (11) and (12) for log-compressed images.
 - (b) *Diffeomorphic demons-based scheme*: The motion field estimation is achieved by minimizing the normalized log-likelihood

(Eq. 2) using the diffeomorphic demons-based scheme (Eq. 18), where the motion transformation, s , is updated by using $s \circ \exp(\mathbf{u})$.

- (c) *Regularization*: The motion and strain estimation is refined by only using reliable information of the myocardial tissue. This is done by using the normalized convolution of Eq. (22) and the probabilistic myocardial tissue characterization calculated in the *Tissue Characterization* phase.

4. *Strain Estimation*: The strain is derived using the classical Cauchy formula:

$$\epsilon = \frac{1}{2} [(\nabla_{\mathbf{x}} s + I)^T (\nabla_{\mathbf{x}} s + I) - I] \quad (24)$$

The longitudinal, circumferential and radial strains are calculated by projecting ϵ on the local cardiac coordinate system.

The algorithm details are described in Algorithm 1.

First the initial deformation \mathbf{s}_0 is set to $\mathbf{0}$ and the local temporal correlation between consecutive images I_t, I_{t-1} is calculated. Then, the set of parameters of the GG mixture model is estimated for $J = 2$ components in *Generalized Gamma Mixture Model*. Specifically, $\pi = \{\pi_1, \pi_2\}$ and $\Theta_j = (a_j, m_j, \beta_j)$ for $j = 1, 2$. Now, the tissue characterizations, \mathbf{Y} , are calculated in *Create Tissue Characterization*. Among all the probabilistic characterizations, only that one of tissue denoted as $\mathbf{Y}_{\text{tiss}} \in \mathbf{Y}$ will be considered for regularization purposes.

Now, the multiresolution scheme can be implemented for n Levels different levels, where $\mathbf{I}_t = \{I_t^i\}_{i=1}^{n\text{Levels}}$, $\mathbf{I}_{t-1} = \{I_{t-1}^i\}_{i=1}^{n\text{Levels}}$ and $\mathbf{Y}_{\text{tiss}} = \{\mathbf{Y}_{\text{tiss}}^i\}_{i=1}^{n\text{Levels}}$ are the sets of images and probabilistic characterization for different resolutions. In each resolution step, the deformation field \mathbf{s}_{i-1} adapted to the dimensions of the image under study I_t^i by spatial interpolation.

Afterwards, the similarity measures between the warped image $I_{t-1}^w = I_{t-1}^i \circ \mathbf{s}_i$ and I_t^i are computed as described in Eqs. (9) and (10) in the case of non-compressed images or Eqs. (11) and (12) for log-compressed images. Thus, the deformation update is calculated by Eq. (18).

The classical demons algorithm considers now a fluid-like regularization of the update with a kernel K_{fluid} . In this step we introduce the probabilistic characterization to avoid contributions of less reliable deformations by means of the normalized convolution. After fluid-like regularization, the diffeomorphic transformation is

Algorithm 1 Diffeomorphic speckle tracking.

```

1: procedure GGSPECKLETRACKING( $I_t, I_{t-1}, nLevels$ )
2:    $\rho \leftarrow LCC(I_t^2, I_{t-1}^2)$  ▷ Eq. (23)
3:    $\Theta \leftarrow GGMixtureModel(I_t, J = 2)$ 
4:    $\Upsilon \leftarrow TissueCharacterization(I_t, \Theta)$  ▷ Eq. (21)
5:    $I_t, I_{t-1}, \Upsilon_{tiss} \leftarrow Pyramid(I_t, I_{t-1}, \Upsilon_{tiss}, nLevels)$ 
6:   for  $i = 1, s_0 = \mathbf{0}; i \geq nLevels; i++$  do
7:      $I_t^i, I_{t-1}^i, \Upsilon_{tiss}^i \leftarrow GetLevel(I_t, I_{t-1}, \Upsilon_{tiss}, i)$ 
8:      $s_i \leftarrow SpatialInterpolation(s_{i-1}, GetDim(I_t^i))$ 
9:     repeat
10:       $I_{t-1}^w \leftarrow I_{t-1}^i \circ s_i$ 
11:      Compute  $\mathbf{u}$  for  $\varphi_{GGS}^s$  or  $\varphi_{GGS}^s$  ▷ Eq. (18)
12:      if fluid-like regularization then
13:         $\mathbf{u} \leftarrow K_{fluid} \otimes (\mathbf{u}, \Upsilon_{tiss}^i)$ 
14:      end if
15:       $c \leftarrow s_i \circ \exp(\mathbf{u})$ 
16:      if diffusion-like regularization then
17:         $s_i \leftarrow K_{diff} \otimes (c, \Upsilon_i)$ 
18:      else
19:         $s_i \leftarrow c$ 
20:      end if
21:    until steady state
22:  end for
23: end procedure

```

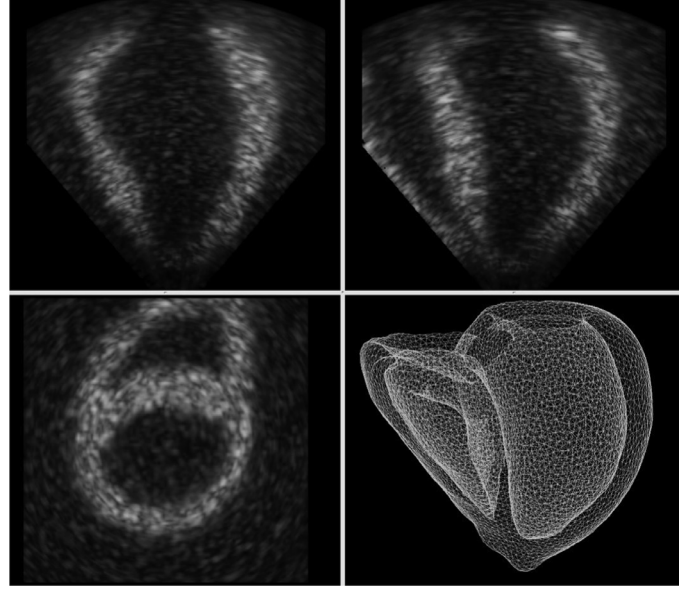


Fig. 2. Benchmark data set *Straus*. Synthetic ultrasound, 3D image for the normal synchronous case without pericardium presented in three orthogonal views. Also the shape model is depicted in the bottom-right corner.

derived as $c = s_i \circ \exp(\mathbf{u})$, which can be efficiently calculated by means of the *fast vector field* algorithm for exponentials proposed in Vercauteren et al. (2009). This transformation can be also smoothed for a diffusion-like regularization, where the probabilistic characterization is again considered.

The deformation field is updated until some steady state is reached, e.g. $\|s_i - s_{i-1}\| \leq TOL$ for some desired tolerance (TOL), and/or a maximum number of iteration.

4. Results

Two sets of experiments are conducted to evaluate the proposed methodology on the synthetic benchmark *Straus* proposed by De Craene et al. (2013). First, the **motion accuracy** is evaluated by studying the spatial motion accuracy at end-systole, the error distribution, the effect of the loss of contrast in the myocardial tissue, and the global displacement error. Second, the strain accuracy is evaluated by studying the global strain accuracy, the spatial strain, according to the 17 segment model recommended by the American Heart Association (AHA), the timing difference for the dyssynchrony case and the loss of contrast for the myocardial tissue. In both cases, the Euclidean distance between the estimation and the ground truth for the left ventricle is used for evaluation.

4.1. Synthetic data

The *Straus* data set provides a realistic 3D geometry of $297 \times 297 \times 297$ pixels with an isotropic resolution of 0.3367 mm (Fig. 2). The ultrasound images were obtained from the segmentation of cine magnetic resonance images, which were used to simulate conventional US images. The data set provides a complex motion in three different scenarios: normal (no lesion), acute ischemia and acute dyssynchrony. The ultrasound speckle structure was synthetically generated by using a sampling at 50 MHz with a phased array transducer centered at 3.3 MHz and transmitting a Gaussian pulse with a -6 dB relative bandwidth of 65%. A symmetric transverse two-way beam profile was assumed, focusing at 80 mm. The simulated images consisted of 107×80 lines in azimuth and elevation direction over an angle of 80×80 degrees, resulting in a frame rate of 30 Hz due to the use of

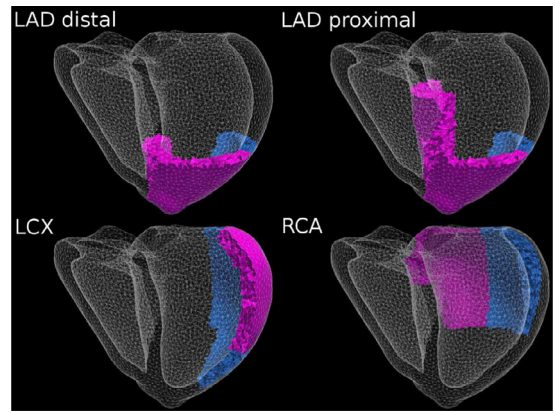


Fig. 3. Ischemic areas used for creating the ischemic cases provided by the data set *Straus*.

parallel beam forming. A set of 16 image sequences was considered. Four ischemic cases were simulated by modifying peak contractility and stiffness values in diseased segments (Fig. 3). For the normal and ischemic cases, the benchmark dataset provides ten image sequences in total, with and without pericardium. Also, three dyssynchrony cases were modeled by progressively removing areas of early activation from the left ventricle (Synchronous, Partial LBBB and Total LBBB). Finally, this dataset includes three extra images where a loss of contrast between the myocardium and blood pool was simulated for the normal case without pericardium. These cases were generated to simulate different signal to noise ratio (SNR) by modifying the relative amplitude of tissue, α , with respect to blood pool scatters (Fig. 4) see De Craene et al. (2013) for further details. A detailed description of the data setup can be found in De Craene et al. (2013).

The proposed methodology is applied to the *Straus* dataset following Algorithm 1, where $nLevels = 3$ and the steady state is reached after a maximum of 30 iterations per level or when the tolerance $TOL = 1e-7$ is reached. The standard deviation values used in the regularization (σ_{fluid} and σ_{diff}) and the maximum step length σ_x (Eq. 18) were determined using an independent linear search between [1, 8] mm for the regularization and [0.5, 5.5] mm for the maximum step. This study shows that the most accurate measures were found for $\sigma_x = 5$ mm, $\sigma_{fluid} = 6$ mm and $\sigma_{diff} = 7.5$ mm. The proposed method

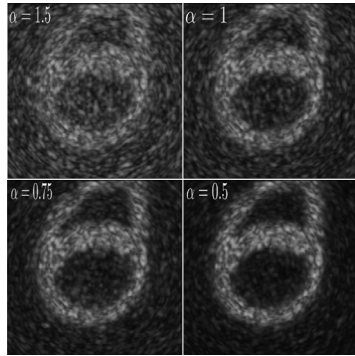


Fig. 4. Example of ultrasound images with different signal-to-noise ratio simulated by modifying the relative amplitude of tissue, α , with respect to blood pool.

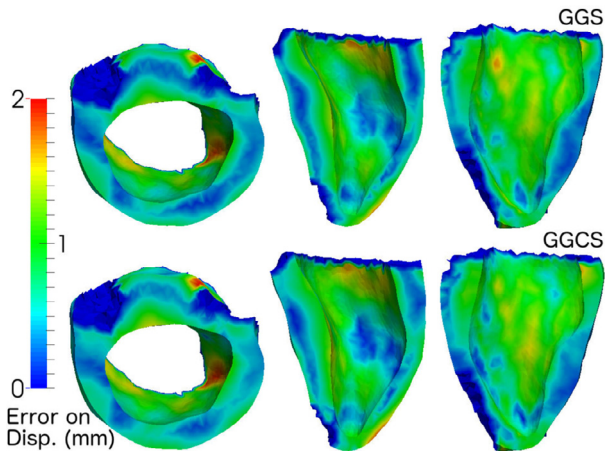


Fig. 5. Spatial motion accuracy at end-systole for the normal synchronous case without pericardium for the proposed methods in three orthogonal views.

was implemented in C++. The time to process a volume in the normal case without pericardium was about 13 min. on a quad-core AMD server 1 GHz with 16 processors. Table 1 shows a detailed description of the runtime and the memory used. The proposed method has not been optimized and these times can be improved.

Table 1

Processing time and memory for a volume corresponding to the normal case without pericardium. GGMM: Runtime for the Generalized Gamma mixture model; Tissue: Runtime for the tissue characterization.

Runtime				Memory
Motion estimation	Temporal correlation	GGMM	Tissue	
13 min	10.5 s	14 s	2 s	448 MB

4.2. Motion accuracy

Spatial motion accuracy: Results for the spatial motion accuracy experiment at end-systole for the normal synchronous case without pericardium are presented in Fig. 5. These results show that both similarity measures, φ_{GGS} (GGS) and φ_{GGCS} (GGCS), have similar displacement error for the normal case without pericardium at end-systole, while the tracking error seems to be spread in basal and mid segments. This effect is mainly due to loss of spatial resolution when the distance increases with respect to the transducer, as stated in De Craene et al. (2013). Furthermore, due to the effect of the regularization, errors are higher in the subendocardial layer of basal and mid segments than inside the myocardium.

To refine this analysis, we compare the displacement error for each ischemic case without pericardium at end-systole, see Fig. 6. A dark grid is plotted over the displacement error for an easier visualization of the ischemic tissue. As expected, the displacement error decreases in the ischemic tissue, where a more stalled motion occurs. On the other hand, in most of the cases, the regularization amplifies the errors at the boundary between healthy and ischemic tissue.

Error distribution: The error distribution is studied by concatenating the average displacement error for each of the 17 AHA segments (boxplots in Fig. 7). For comparison purposes, we include the motion accuracy of the classical diffeomorphic demons (efficient second-order minimization) method proposed in Vercauteren et al. (2009) (named Diff in this work) and the different speckle tracking methods previously described in Section 2: Philips, Creatis, KU Lueven, UPF and Mevis.

First, note that the displacement errors shown in Fig. 7 (GGS and GGCS) are higher at late diastole than in the early diastole phase, due to the design decision of preserving the temporal resolution instead of avoiding the frame to frame error accumulation. The highest error

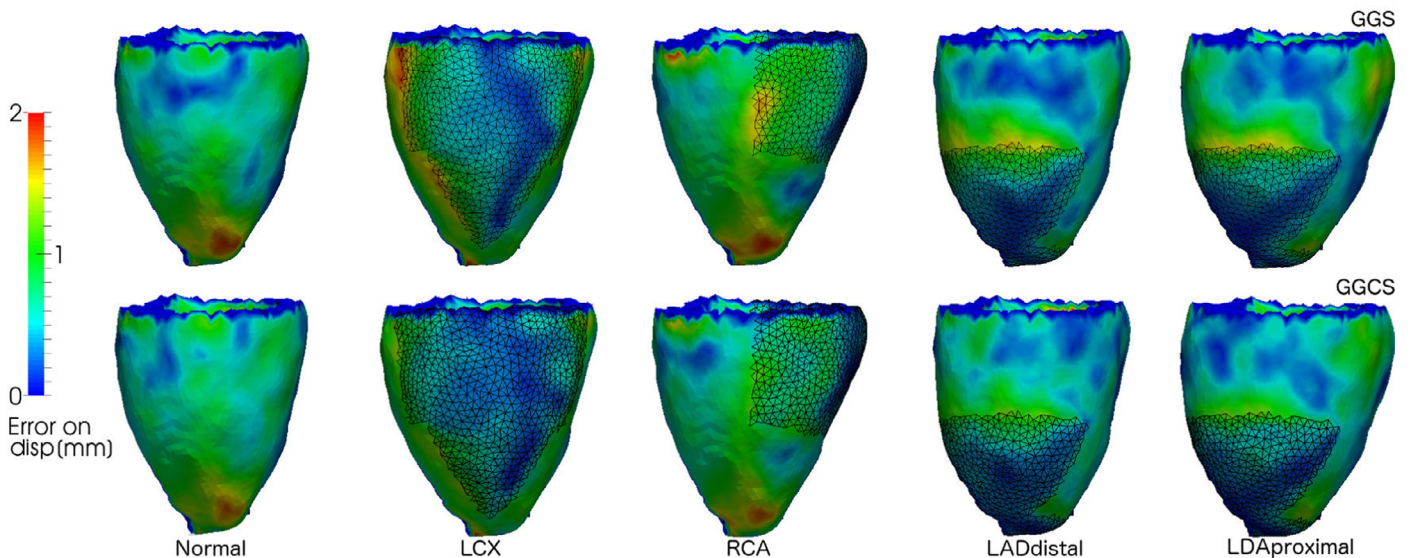


Fig. 6. Spatial motion accuracy at end-systole for ischemic LCX cases without pericardium for the proposed methods. A dark grid is plotted over the displacement error for an easier visualization of the ischemic segments.

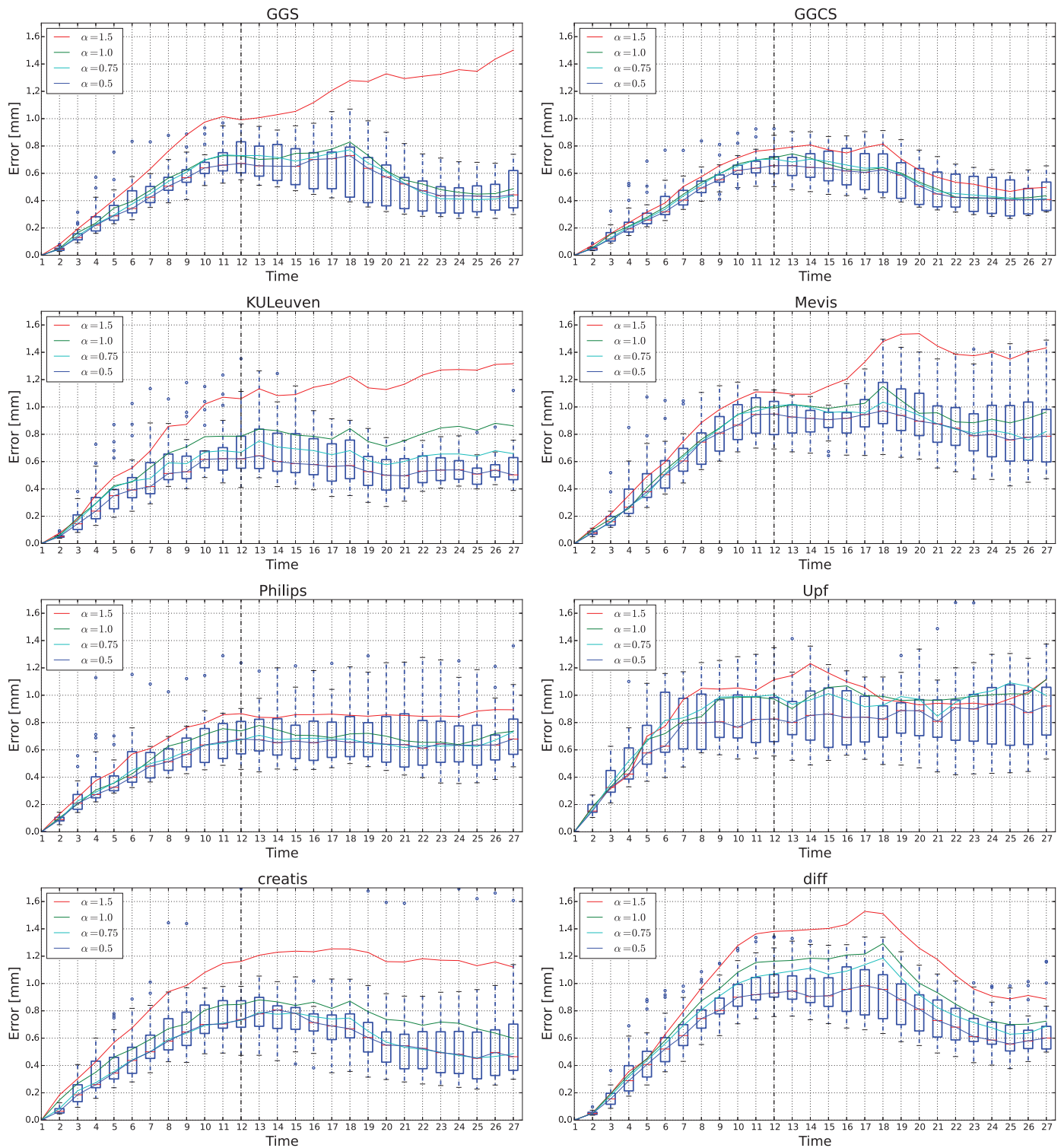


Fig. 7. Motion error along the cardiac phase for different signal to noise ratio. The boxplot corresponds to the highest signal to noise ratio ($\alpha = 0.5$) for the normal synchronous case without pericardium. The color curves show the evolution of the median error along the cardiac phase for a different signal to noise ratio. The cardiac frame at end-systole is show as vertical dash line.

shown for the normal case at different SNR values is found two frames after end-systole for the similarity measure GGCS; and six frames after end-systole for GGS. Similar results are found for KULeuven, Creatis, Philips, Diff and Mevis at frames 13, 14, 14, 17 and 18 respectively. For the proposed methods, there is an increase of the variance after end-systole (shown as a vertical dash line in Fig. 7) that is generated by the error accumulation. On the other hand, note that, for both

methods, the maximum error is not located on the same frame. Since the same parameters have been used in both methods, this difference can only be explained by the compression used in the speckle model, that affects each method differently.

Effect of the loss of contrast: Next, we study the effect of a loss of contrast between the myocardium and the blood pool. The loss of contrast is directly related to a decay in the SNR. See, for instance,

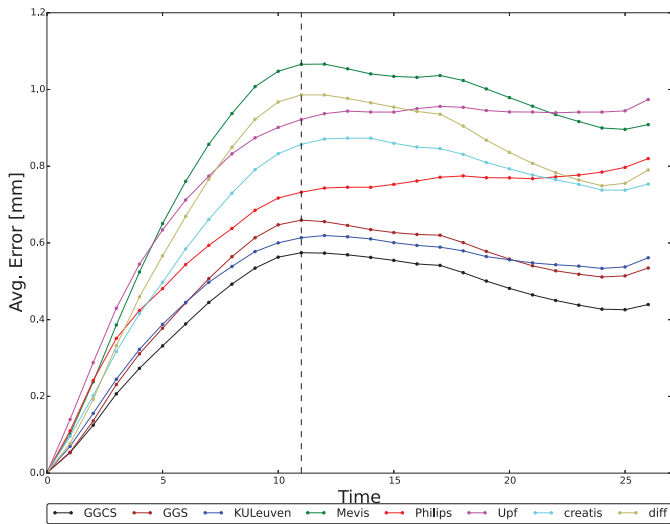


Fig. 8. Global average motion error for all the cases by method. The vertical dash line corresponds to the cardiac frame at end-systole.

the example depicted in Fig. 4, where the myocardium and blood are easier identified for the $\alpha = 0.5$ case.

Fig. 7 plots the median accuracy curves from the highest SNR ($\alpha = 0.5$) to the lowest ($\alpha = 1.5$). As expected, the displacement error is higher when a loss of contrast occurs, i.e. for the lowest SNR. According to the results, the proposed method GGCS is the most accurate and robust method in terms of minimum error for all the SNR considered. When a high SNR scenario is considered, i.e. $\alpha = 0.5$, other methods show a similar behavior in terms of median error, as GGS and KULeuven. Furthermore, Philips and the proposed methods show a median error preservation for the different SNR levels with the exception of the lowest SNR, i.e. from $\alpha = 0.5$ to $\alpha = 1.0$. These three methods are the only ones with a median error (with the exception of the lowest SNR) below the third quartile of the higher SNR ($\alpha = 0.5$).

The different behavior of GGS and GGCS at the lowest SNR, can be explained by the logarithmic compression assumed in the underlying speckle model. In this case, the logarithmic compression transforms the ratio of intensity into a difference which is less sensitive to the loss of SNR.

Global displacement error: The displacement error is studied along the cardiac phase and globally. The global motion accuracy (Fig. 9) is measured by concatenating the average displacement error for each segment at all time points for all datasets within a group: ischemy (5 sequences), ischemy without pericardium (5 sequences) and dyssynchrony (3 sequences). Also, global motion accuracy is measured along the entire cardiac phase by concatenating the average displacement error for each of the 17 segments for all datasets (Fig. 8).

According to Figs. 9 and 8, the proposed method GGCS shows the best motion accuracy for the ischemic case with and without pericardium (median error of 0.42 and 0.4 mm, respectively); and it also provides a remarkable motion accuracy for the dyssynchrony case (median error of 0.46 mm). Moreover, these results show that the proposed method GGS is close to the best motion accuracy, 0.48 mm for the ischemic case with and without pericardium; and 0.54 mm for the dyssynchrony case, only overtaken by the GGCS and KULeuven.

An interesting result is obtained when the results for the two ischemic groups are compared. Methods that use a myocardial tissue segmentation, GGS, GGCS, KULeuven and Philips, are more robust to the pericardium inclusion, as expected. In addition, GGS and GGCS,

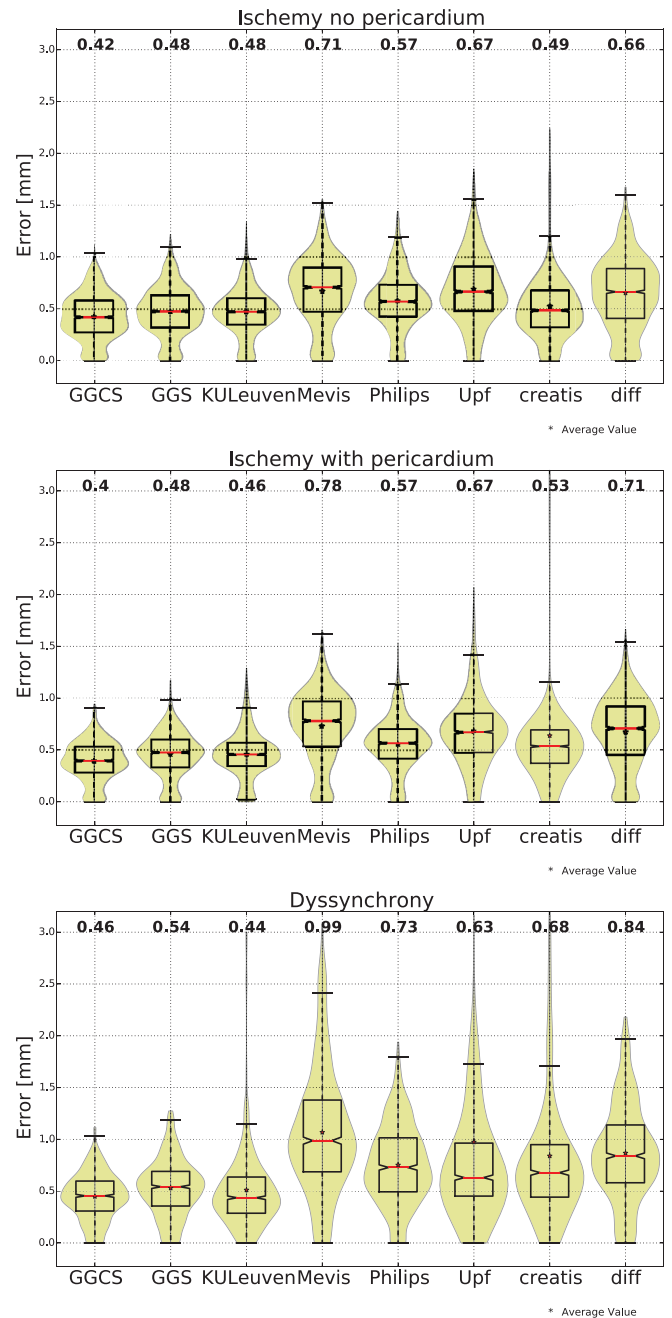


Fig. 9. Global displacement accuracy for all datasets within a group: ischemy without pericardium (5 sequences), ischemy (5 sequences) and dyssynchrony (3 sequences).

present the advantage of using an automatic tissue characterization. Despite the UPF method shows no difference between both ischemic groups for the median error, the violin plot reveals that the error distribution changes and becomes centered around the median for the ischemic case with pericardium. In contrast, the error distribution for the proposed methods (GGS and GGCS), KULeuven and Philips remain the same. Another interesting result is obtained by comparing the ischemic and dyssynchrony groups. It is observed that all the methods tend to increase the error for the dyssynchrony cases, mainly caused by an excessive regularization. As it was stated in De Craene et al. (2013) this error increase cannot be attributed to image quality since ultrasound simulation parameters were kept identical in the two groups. In addition, the violin plot for the dyssynchrony group reveals that the error probability density seems to be more centered

Table 2

Global strain accuracy for all methods. Mean and standard deviation errors are reported for all dataset at all data points. The best values are in bold (best value + 0.3%)

	Radial error [%] $\mu \pm SD$	Circ. error [%] $\mu \pm SD$	Long. error [%] $\mu \pm SD$
GGS	7.1 ± 4.9	2.1 ± 1.1	2.1 ± 1.3
GGCS	7.9 ± 6.2	2.0 ± 0.9	2.2 ± 1.3
KULeuven	7.1 ± 4.9	2.2 ± 1.1	2.7 ± 1.8
diff	8.5 ± 6.7	2.3 ± 1.2	2.3 ± 1.7
Mevis	8.3 ± 6.3	2.9 ± 1.7	3.0 ± 2.5
Philips	9.9 ± 7.1	2.5 ± 1.3	2.8 ± 2.1
Upf	9.7 ± 6.3	3.8 ± 2.4	4.0 ± 5.4
creatis	8.8 ± 8.1	2.5 ± 1.3	3.0 ± 2.7

around the median for the proposed methods (GGS and GGCS) and Mevis with respect to the ischemic cases (Fig. 9). These results show that the average error for the dyssynchrony cases increased considerably with respect to the ischemic cases for all methods with the exception of the proposed methods (GGS and GGCS) and the KULeuven.

4.3. Strain accuracy

Global strain accuracy: The global strain accuracy is evaluated by concatenating the average strain error for each of the 17 AHA segments for cardiac phases and all datasets. Results are shown in Table 2. In Table 3 we have detailed the strain accuracy within three groups: ischemic case without pericardium, ischemic case with pericardium and dyssynchrony case.

According to the results, the best accuracy for the radial strain was provided by GGS and KULeuven. However, this accuracy is too low to be used for discriminating healthy from diseased segments. The low accuracy for the radial strain is due to the fact that the torsional and longitudinal motion provided by the benchmark are higher than the myocardial compression. Therefore, the regularization used by the methods will reduce the compression and it will increase the radial error.

The longitudinal strain, on the other hand, can only be used for the proposed methods (GGS and GGCS), Philips and KULeuven, since these methods are the only ones having a standard deviation around 2%, which is appropriate to be used for discrimination purposes (Table 3 Dyssynchrony case). However, the normal longitudinal strain provided by the Straus benchmark presents low values

Table 3

Global strain accuracy for all methods. Mean and standard deviation errors are reported for all dataset at all data points by group: ischemy without pericardium, ischemy with pericardium and dyssynchrony. The best values are in bold (best value + 0.3%)

	Radial error ($\mu \pm SD$) [%]			Circ. error ($\mu \pm SD$) [%]			Long. error ($\mu \pm SD$) [%]		
	Isch. no pc.	Isch. with pc.	Dyssynchrony	Isch. no pc.	Isch. with pc.	Dyssynchrony	Isch. no pc.	Isch. with pc.	Dyssynchrony
GGS	7.1 ± 4.8	6.5 ± 4.5	8.3 ± 5.7	2.1 ± 0.9	2.0 ± 0.9	2.3 ± 1.6	2.2 ± 1.3	2.0 ± 1.2	2.1 ± 1.3
GGCS	7.8 ± 6.4	7.0 ± 5.6	10.1 ± 6.8	2.0 ± 0.9	1.9 ± 0.9	2.0 ± 1.0	2.3 ± 1.4	2.2 ± 1.3	1.9 ± 1.1
KULeuven	7.3 ± 5.0	6.7 ± 4.3	7.8 ± 5.9	2.1 ± 1.0	2.2 ± 1.1	2.1 ± 1.1	2.7 ± 1.8	2.9 ± 1.9	2.5 ± 1.4
diff	8.3 ± 6.9	7.6 ± 6.0	10.8 ± 7.1	2.2 ± 1.1	2.3 ± 1.2	2.4 ± 1.4	2.1 ± 1.3	2.1 ± 1.3	3.2 ± 2.7
Mevis	8.4 ± 6.5	7.6 ± 5.9	9.8 ± 6.5	2.8 ± 1.3	2.8 ± 1.4	3.4 ± 2.5	2.7 ± 1.6	2.7 ± 1.7	4.3 ± 4.5
Philips	9.1 ± 6.2	9.2 ± 6.0	13.1 ± 9.9	2.5 ± 1.3	2.4 ± 1.3	2.5 ± 1.5	2.7 ± 1.9	2.9 ± 2.2	2.7 ± 2.2
Upf	9.3 ± 5.7	10.3 ± 6.6	9.5 ± 6.5	3.9 ± 2.2	3.8 ± 2.3	3.7 ± 3.0	3.3 ± 2.0	3.4 ± 2.2	6.9 ± 11.4
creatis	8.3 ± 6.8	8.8 ± 9.6	10.0 ± 7.0	2.3 ± 1.0	2.6 ± 1.3	2.9 ± 1.6	2.6 ± 1.5	2.9 ± 2.0	3.9 ± 4.9

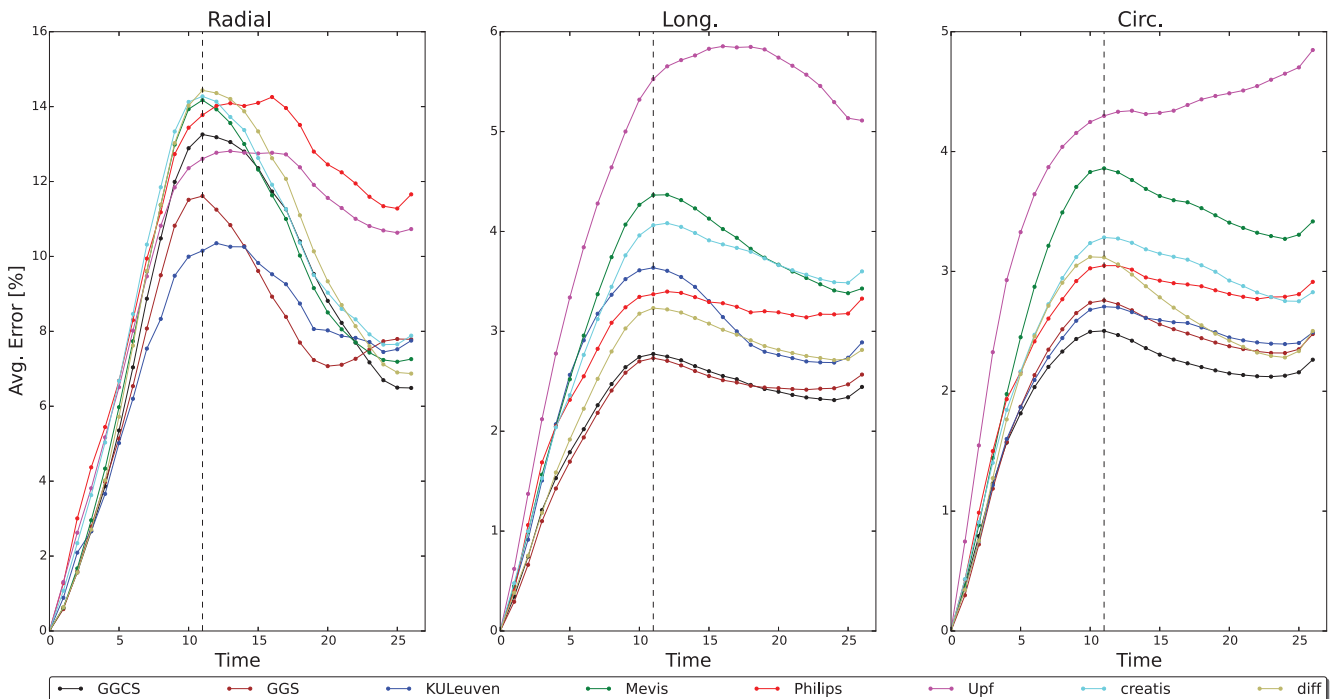


Fig. 10. Global average accuracy for radial (Radial), longitudinal (Long.) and circumferential strain (Circ.) by method. The vertical dash line corresponds to the cardiac frame at end-systole.

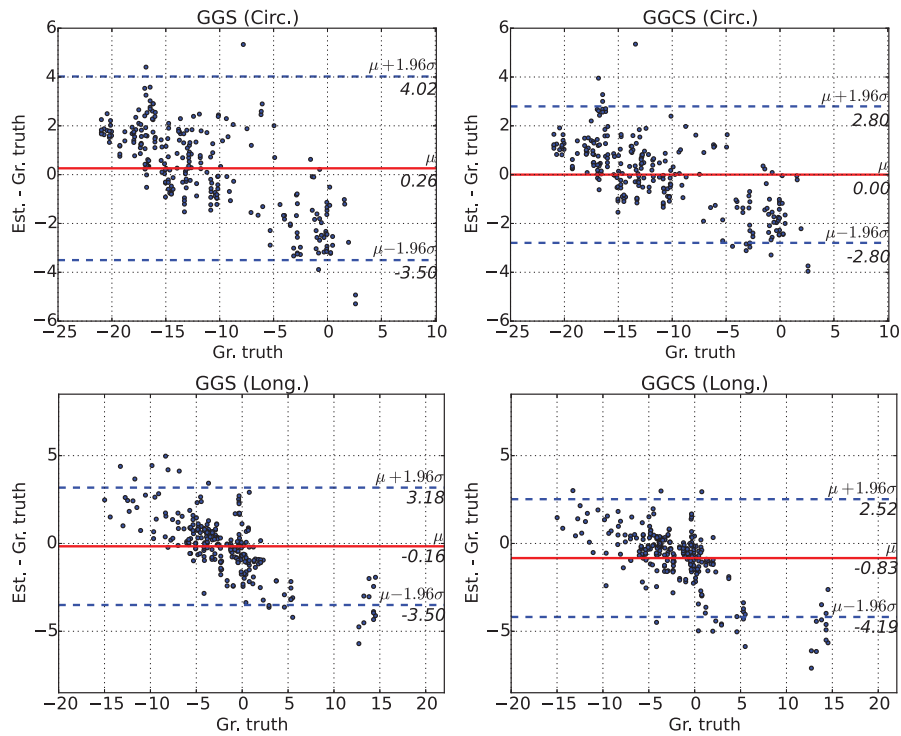


Fig. 11. End-systolic Bland–Altman plots of circumferential (top) and longitudinal (bottom) strain for the proposed methods (GGS and GGCS).

with respect to normal deformation ranges reported in the literature, thus, the longitudinal strain is also excluded for discriminating purpose.

Finally, the proposed methods show similar accuracy for the circumferential strain (Fig. 10). In contrast to radial and longitudinal strain, all methods show a high accuracy level for the circumferential strain (a standard deviation around 2% or less) which suffices to be used for discrimination purposes.

The average strain error is studied for the entire cardiac phase (Fig. 10). Results suggest that GGS and GGCS are the most accurate methods to measure the longitudinal and circumferential strain. Despite presenting very similar results, GGCS shows better longitudinal and circumferential accuracy than GGS. In contrast, GGCS presents a lower radial accuracy than GGS, which has a high radial accuracy with respect to the methods studied.

The highest global strain error was found at end-systole as expected, since the highest global displacement error is located there. In addition, the Bland–Altman plots (Fig. 11) reveal a small bias for the proposed methods GGS and GGCS (0.26 and 0% for the circumferential strain, and -0.16 and -0.83% for the longitudinal strain respectively). These plots were created by concatenating the average strain in each segment for all dataset (except ones at low SNRs).

Spatial strain accuracy: The spatial strain distribution is studied within the 17 segment model using the “bull’s eye” maps. These results are presented in Figs. 12 and 13. The resulting maps for the normal case show that the proposed method with the GGS similarity measure is more accurate than the GGCS for radial and longitudinal strain while they both have similar circumferential strain, as described in the previous section, *Global strain accuracy*. Moreover, this result reveals an underestimation of the radial strain by GGS and GGCS.

By comparing the bull’s eye map for the LCX and LADdist ischemic cases without pericardium (Figs. 12 and 13), there is no doubt that the ischemic segments are well discriminated by the circumferential

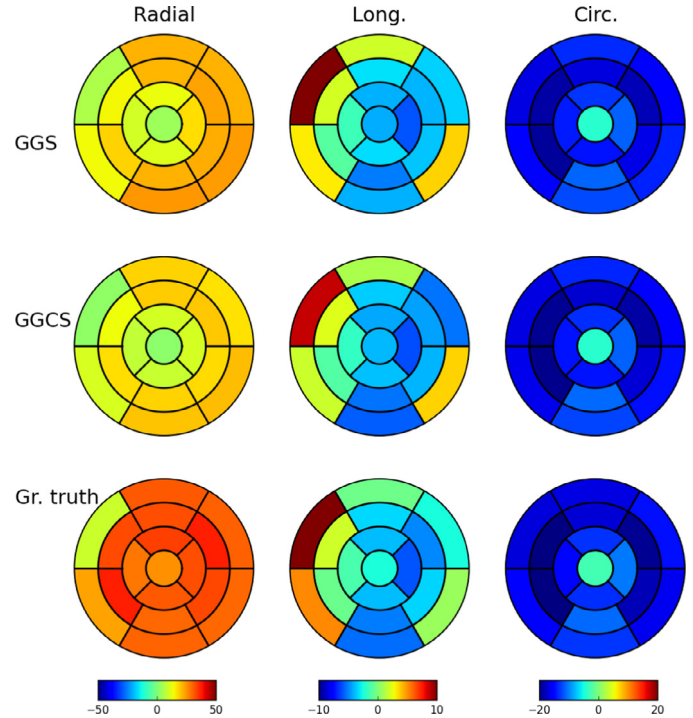


Fig. 12. End-systolic strain values of the normal case without pericardium for the proposed methods (GGS and GGCS) and the ground truth. The strain values were grouped by the 17 segment model.

strain. These segments show a difference of more than 10% for circumferential strain. A lower difference was found for the longitudinal strain (less than 5%), though, these segments are also properly distinguished. The small bias and standard deviation error (Fig. 11 and Tables 2 and 3) confirm the visual results.

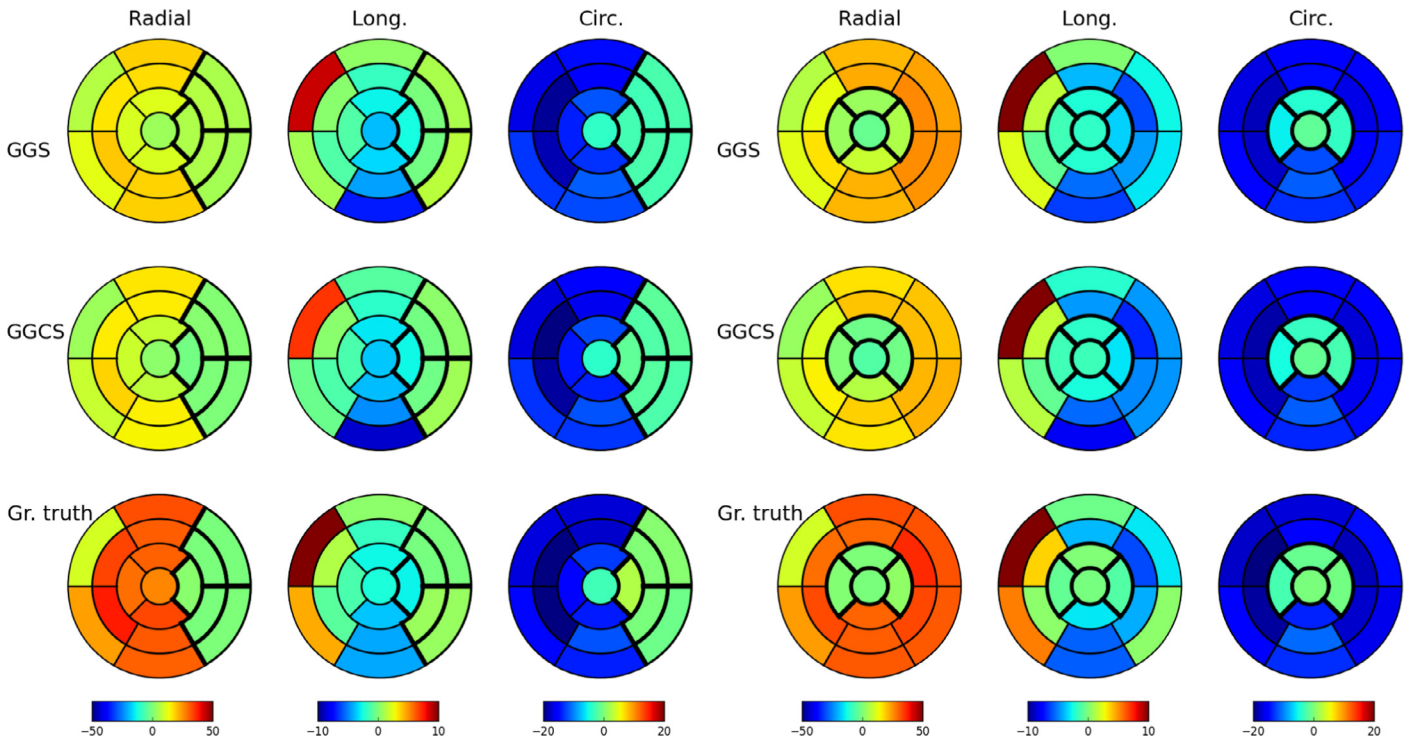


Fig. 13. End-systolic strain values of the LCX (left) and LADdist (right) ischemic cases without pericardium for the proposed methods (GGS and GGCS) and the ground truth. The strain values were grouped by the 17 segment model and the ischemic segments are outlined in bold.

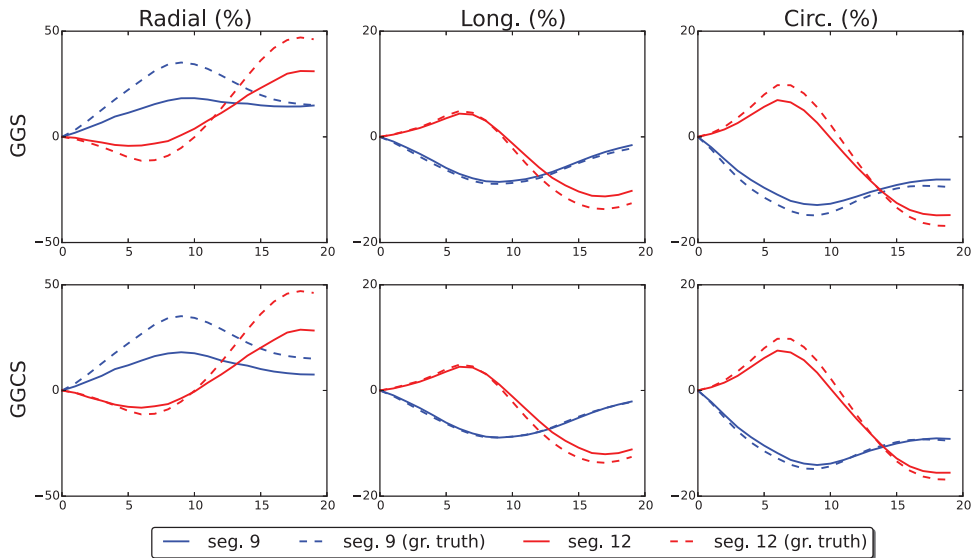


Fig. 14. Radial, longitudinal and circumferential, strain of the Total LBBB ischemic case without pericardium for the segments 9 and 12 according to the 17 segment model. The ground truth is presented in dash line.

Timing difference: In order to study dyssynchrony pathologies, the strain curves for two opposed segments at mid-level are depicted in Fig. 14. For the sake of comparison, only the inferoseptal and antero-lateral (segments 9 and 12) were considered. The strain curves are obtained from the Total LBBB dyssynchrony case with the goal to identify the timing difference and the possibility to recover the timing difference between the dyssynchronous walls. In the radial direction, time-to-peaks values were not accurate enough for quantifying the dyssynchrony due to an underestimation of radial strain. However, longitudinal and circumferential strain are good enough for observing delays between septal and lateral strain curves.

Effect of the loss of contrast: Last, similar to the motion estimation, we study the effect of the loss of contrast between the myocardium and the blood pool for the circumferential, longitudinal and radial strain. The absolute error was concatenated for all data points and all times to make a boxplot for each SNR value (Fig. 15). Generally, all methods show an error increase when the contrast becomes too low, i.e. $\alpha = 1.5$. GGS, GGCS, KULeuven and Philips seem to be the most robust methods due to the median preservation for different SNR values. However, the highest strain accuracy was achieved by GGS and GGCS for the circumferential and longitudinal strain. In particular, the radial strain showed a high sensibility to the different SNR

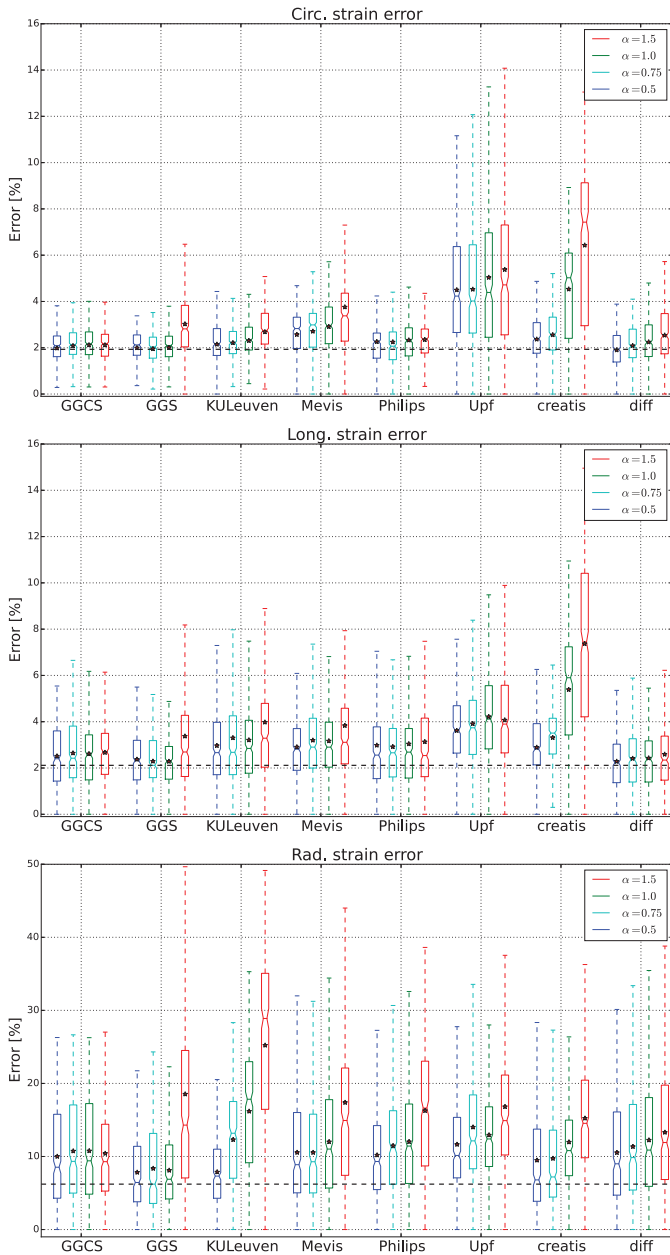


Fig. 15. Circumferential, longitudinal and radial strain accuracy at different signal to noise ratio by method.

for all method with the exception of the proposed method with the similarity measure GGCS.

5. Conclusions

In this paper, we have proposed a maximum likelihood diffeomorphic speckle tracking method for 3D strain estimation which is applied for detection of the regional abnormal areas through regional myocardial strain assessment. Unlike previous maximum likelihood approaches, our method proposes a more realistic speckle model with the inclusion of an adaptive temporal correlation between consecutive frames. Also, we provide a formulation that generalizes conventional speckle models (Rayleigh, Nakagami and Gamma) into one more versatile and adaptable model for real data. This approach makes use of a probabilistic myocardial tissue characterization to distinguish between more and less reliable myocardial motion; a bivariate Generalized Gamma speckle model to provide a more realistic

speckle model, which considers the temporal correlation between frames; and a maximum likelihood methodology to provide a diffeomorphic motion estimation implemented in an efficient demons-like formulation, which allows to perform the registration before and after log-compression. For accuracy and agreement assessment, the proposed method for both similarity measures (GGS and GGCS) were evaluated in a total of 16 image sequences grouped in three scenarios: normal (no lesion), acute ischemia and acute dyssynchrony. Additionally, the motion and strain accuracy were compared with six other speckle tracking methods.

For the experiments we conducted, our method produced the best results in comparison to other methods for assessing motion and strain. Also, the results indicate that the proposed diffeomorphic speckle tracking method provides robust motion and strain estimation for different SNR levels.

Among all compared methods, the proposed one had the highest displacement accuracy with an average global median error of 0.42 mm for the similarity measure GGCS. A similar motion accuracy was observed for the similarity measure GGS with an average median error of 0.5 mm. This difference is due to the log-compression assumed into the underlying speckle model for the similarity measure GGCS. In this case, the log-compression transforms the ratio of intensity into a difference which is more appropriate for motion due to its numerical robustness in comparison to the ratio of image intensities. However, the median error preservation for the different SNR levels shows that the similarity measure GGS is one of the most robust methods, which evidences the adequacy of the GG speckle model for speckle tracking.

Regarding strain, it was observed that the proposed method tended to underestimate the radial strain. However, the global strain accuracy reveals that the proposed method GGS is the most accurate method to measure the radial strain with a median error of $7.1 \pm 4.9\%$, follows by the GGCS ($7.9 \pm 6.2\%$). The low accuracy for the radial strain is due to the fact that the torsional and longitudinal motion provided by the benchmark is higher than the myocardial compression. The longitudinal and circumferential strain were accurately quantified for the proposed methods with a median error of $2.1 \pm 1.3\%$ and $2.2 \pm 1.3\%$ (GGS and GGCS); and $2.1 \pm 1.1\%$ and $2.0 \pm 0.9\%$ (GGS and GGCS) for longitudinal and circumferential strain. The study of regional abnormal areas reveals that the proposed methods GGS and GGCS are capable of identifying abnormal segments for a reduced cardiac function by measuring the circumferential and longitudinal strain. Furthermore, both strain measures are capable to detect the timing difference for the dyssynchrony cases. Finally, the study of different SNR values shows that the proposed method is the most robust for measuring the longitudinal and circumferential strain.

Acknowledgments

This work was partially supported by the Ministerio de Educación, Ciencia y Tecnología (MECyT) de Argentina, the Fundación Carolina de España, the Universidad de Valladolid (FPI-Uva) and the Ministerio de Ciencia e Innovación de España for grant TEC 2013–44194. Gonzalo Vegas-Sánchez-Ferrero acknowledges Consejería de Educación, Juventud y Deporte of Comunidad de Madrid and the People Programme (Marie Curie Actions) of the European Union's Seventh Framework Programme (FP7/2007–2013) for REA grant agreement no. 291820.

Appendix A. Bivariate Generalized Gamma similarity measure (GGS)

The similarity measure φ_{GGS} is derived from Eq. (4) as follows:

$$\varphi_{GGS}^s = -\log\left(\frac{1}{I_t(\mathbf{x})} p_\eta(\eta)\right)$$

$$\begin{aligned}
&= -\log\left(\frac{\beta 2^{2m-1} \Gamma(m+0.5)}{\sqrt{\pi} (1-\rho)^{-\beta} \Gamma(m)}\right) \\
&+ \log(I_t(\mathbf{x})) - \log\left(\frac{\eta^{2\beta m-1}}{(\eta^{2\beta} + 1)^{2m}}\right) \\
&- \log\left(\left(\frac{(\eta^{2\beta} + 1)^2 - 4\rho\eta^{2\beta}}{(\eta^{2\beta} + 1)^2}\right)^{-\frac{2m+1}{2}}\right) \\
\varphi_{\text{GGS}}^s &= -\log\left(\frac{\beta 2^{2m} \Gamma(m+0.5)}{\sqrt{\pi} (1-\rho)^{-\beta} \Gamma(m)}\right) \\
&+ \log(I_t(\mathbf{x})) - (2\beta m - 1) \log(\eta) \\
&+ \frac{2m+1}{2} \log((\eta^{2\beta} + 1)^2 - 4\rho\eta^{2\beta}) \\
&- \log(\eta^{2\beta} + 1) \\
&+ m \log\left(\left(\frac{e^{2\beta\eta} + 1}{2e^{\beta\eta}}\right)^2\right) \\
&+ \frac{2m+1}{2} \log\left(1 - \frac{\rho}{\left(\frac{e^{2\beta\eta} + 1}{2e^{\beta\eta}}\right)^2}\right) \\
&= -\log\left(\frac{\beta 2^{2m-1} \Gamma(m+0.5)}{\sqrt{\pi} (1-\rho)^{-\beta} \Gamma(m)}\right) - m \log(4) \\
&+ m \log(\cosh^2(\beta\eta)) \\
&+ \frac{2m+1}{2} \log\left(\frac{\cosh^2(\beta\eta) - \rho}{\cosh^2(\beta\eta)}\right) \\
&= -\log\left(\frac{\beta 2^{2m-1} \Gamma(m+0.5)}{\sqrt{\pi} (1-\rho)^{-\beta} \Gamma(m)}\right) - m \log(4) \\
&+ \frac{2m+1}{2} \log(\cosh^2(\beta\eta) - \rho) \\
&- \frac{1}{2} \log(\cosh^2(\beta\eta))
\end{aligned}$$

where p_η is the probability density function for the ratio of two correlated Generalized Gamma random variables and $\eta = \frac{I_{t-1} \circ s(\mathbf{x})}{I_t(\mathbf{x})}$ is the ratio of two random variables. After adding the compensation term to remove the bias of the similarity measure when the optimal transformation is found, and removing constant values, the similarity measure (Eq. (9)) is as follows:

$$\begin{aligned}
\varphi_{\text{GGS}}^s &= \log(I_t(\mathbf{x})) - (2\beta m - 1) \log(\eta) \\
&+ \frac{2m+1}{2} \log((\eta^{2\beta} + 1)^2 - 4\rho\eta^{2\beta}) \\
&- \log(\eta^{2\beta} + 1)
\end{aligned}$$

Finally, the gradient of the similarity measure with respect to the transformation $s(\mathbf{x})$ is derived as follow:

$$\begin{aligned}
\nabla \varphi_{\text{GGS}}^s &= \left[-\frac{2\beta m - 1}{\eta I_t(\mathbf{x})} + \frac{(2m+1)}{2((\eta^{2\beta} + 1)^2 - 4\rho\eta^{2\beta})} \right. \\
&\cdot \left(\frac{2(\eta^{2\beta} + 1)2\beta\eta^{2\beta-1}}{I_t(\mathbf{x})} - \frac{4\rho 2\beta\eta^{2\beta-1}}{I_t(\mathbf{x})} \right) \\
&\left. - \frac{2\beta\eta^{2\beta-1}}{I_t(\mathbf{x})} - \frac{1}{I_{t-1}(\mathbf{x})} \right] \nabla J \\
&= \left[-\frac{2\beta m}{I_{t-1}(\mathbf{x})} - \frac{2\beta\eta^{2\beta}}{(\eta^{2\beta} + 1)I_{t-1}(\mathbf{x})} \right. \\
&\left. + \frac{2m+1}{2} \frac{2\beta\eta^{2\beta}}{I_{t-1}(\mathbf{x})} \frac{2(\eta^{2\beta} + 1) - 4\rho}{(\eta^{2\beta} + 1)^2 - 4\rho\eta^{2\beta}} \right] \nabla J
\end{aligned}$$

where $\nabla J = \frac{1}{2}(\nabla I_t + \nabla I_{t-1} \circ s)$ that leads to an efficient second order minimization.

Appendix B. Bivariate Generalized Gamma similarity measure with compression (GGCS)

The similarity measure φ_{GGCS} is derived taking into account the image compression into Eq. (6) as follows:

$$\begin{aligned}
\varphi_{\text{GGCS}}^s &= -\log(\hat{\eta} p_\eta(\hat{\eta})) \\
&= -\log\left(\frac{\beta 2^{2m-1} \Gamma(m+0.5)}{\sqrt{\pi} (1-\rho)^{-\beta} \Gamma(m)}\right) \\
&- m \log\left(\frac{\hat{\eta}^{2\beta}}{(\hat{\eta}^{2\beta} + 1)^2}\right) \\
&+ \frac{2m+1}{2} \log\left(1 - \frac{4\rho\hat{\eta}^{2\beta}}{(\hat{\eta}^{2\beta} + 1)^2}\right) \\
\varphi_{\text{GGCS}}^s &= -\log\left(\frac{\beta 2^{2m-1} \Gamma(m+0.5)}{\sqrt{\pi} (1-\rho)^{-\beta} \Gamma(m)}\right) - m \log(4)
\end{aligned}$$

where $\eta = e^{\hat{\eta}}$. By removing constant values, the similarity measure is:

$$\begin{aligned}
\varphi_{\text{GGCS}}^s &= \frac{2m+1}{2} \log(\cosh^2(\beta\eta) - \rho) \\
&- \frac{1}{2} \log(\cosh^2(\beta\eta))
\end{aligned}$$

Finally, the gradient of the similarity measure with respect to the transformation $s(\mathbf{x})$ is derived as follow:

$$\begin{aligned}
\nabla \varphi_{\text{GGCS}}^s &= \left((2m+1) \frac{\cosh(\beta\eta) \sinh(\beta\eta) \beta}{\cosh^2(\beta\eta) - \rho} \right. \\
&\left. - \frac{\cosh(\beta\eta) \sinh(\beta\eta) \beta}{\cosh^2(\beta\eta)} \right) \nabla J \\
&= \left(\frac{2m+1}{\cosh(\beta\eta) - \rho} - \frac{1}{\cosh^2(\beta\eta)} \right) \\
&\cdot \cosh(\beta\eta) \sinh(\beta\eta) \beta \nabla J
\end{aligned}$$

where $\nabla J = \frac{1}{2}(\nabla I_t + \nabla I_{t-1} \circ s)$ that leads to an efficient second order minimization.

References

- Abraham, T.P., Dimaano, V.L., Liang, H.-Y., 2007. Role of tissue Doppler and strain echocardiography in current clinical practice. *Circulation* 116 (22), 2597–2609.
- Alessandrini, M., Liebgott, H., Barbosa, D., Bernard, O., 2013. Monogenic phase based optical flow computation for myocardial motion analysis in 3d echocardiography. In: Camara, O., Mansi, T., Pop, M., Rhode, K., Sermesant, M., Young, A. (Eds.), *Statistical Atlases and Computational Models of the Heart. Imaging and Modelling Challenges*, vol. 7746. Lecture Notes in Computer Science. Springer, Berlin Heidelberg, pp. 159–168.
- Amundsen, B.H., Helle-Valle, T., Edvardsen, T., Torp, H., Crosby, J., Lyseggen, E., et al., 2006. Noninvasive myocardial strain measurement by speckle tracking echocardiography: validation against sonomicrometry and tagged magnetic resonance imaging. *J. Am. Coll. Cardiol.* 47 (4), 789–793.
- Beauchemin, S.S., Barron, J.L., Sep. 1995. The computation of optical flow. *ACM Comput. Surv.* 27 (3), 433–466.
- Bithas, P.S., Sagias, N.C., Tsiftsis, T.A., Karagiannidis, G.K., 2007. Distributions involving correlated generalized gamma variables. *Proc. Int. Conf. App. Stochastic Models Data Anal.* vol. 12.
- Bohs, L., Geiman, B., Anderson, M., Gebhart, S., Trahey, G., 2000. Speckle tracking for multi-dimensional flow estimation. *Ultrasound*. 38 (1–8), 369–375.
- Burckhardt, C., 1978. Speckle in ultrasound b-mode scans. *IEEE Trans. Sonics Ultrason.* 25 (1), 1–6.
- Byrd, R., Lu, P., Nocedal, J., Zhu, C., 1995. A limited memory algorithm for bound constrained optimization. *SIAM J. Sci. Comput.* 16 (5), 1190–1208.
- Cohen, B., Dinstein, I., 2002. New maximum likelihood motion estimation schemes for noisy ultrasound images. *Pattern Recognit.* 35 (2), 455–463.
- Curiale, A.H., Vegas-Sánchez-Ferrero, G., Aja-Fernández, S., 2013. Speckle tracking in interpolated echocardiography to estimate heart motion. In: Ourselin, S., Rueckert, D., Smith, N. (Eds.), *Functional Imaging and Modeling of the Heart*, vol. 7945. Lecture Notes in Computer Science. Springer, Berlin, Heidelberg, pp. 325–333.

- Dandel, M., Lehmkuhl, H., Knosalla, C., Suramelašvili, N., Hetzer, R., 2009. Strain and strain rate imaging by echocardiography – basic concepts and clinical applicability. *Curr. cardiol. rev.* 5 (2), 133–148.
- De Craene, M., Marchesseau, S., Heyde, B., Gao, H., Alessandrini, M., Bernard, O., et al., 2013. 3d strain assessment in ultrasound (Straus): a synthetic comparison of five tracking methodologies. *IEEE Trans. Med. Imag.* PP (99), 1–1.
- Helle-Valle, T., Crosby, J., Edvardsen, T., Lyseggen, E., Amundsen, B.H., Smith, H.-J., et al., 2005. New noninvasive method for assessment of left ventricular rotation. *Circulation* 112 (20), 3149–3156.
- Heyde, B., Barbosa, D., Claus, P., Maes, F., D'hooge, J., 2013. Three-dimensional cardiac motion estimation based on non-rigid image registration using a novel transformation model adapted to the heart. In: Camara, O., Mansi, T., Pop, M., Rhode, K., Sermesant, M., Young, A. (Eds.), *Statistical Atlases and Computational Models of the Heart. Imaging and Modelling Challenges*, vol. 7746. *Lecture Notes in Computer Science*. Springer, Berlin, Heidelberg, pp. 142–150.
- Knutsson, H., Andersson, M., sept. 2005. Morphons: segmentation using elastic canvas and paint on priors. *IEEE Int. Conf. on Image Process* 2 (II), 1226–1229.
- Knutsson, H., Westin, C., jun 1993. Normalized and differential convolution: Methods for interpolation and filtering of incomplete and uncertain data. In: *Computer Vision and Pattern Recognition. Proceedings CVPR '93*, 1993 IEEE Computer Society Conference on, pp. 515–523.
- Konofagou, E., Ophir, J., 1998. A new elastographic method for estimation and imaging of lateral displacements, lateral strains, corrected axial strains and poisson's ratios in tissues. *Ultrasound Med. Biol.* 24 (8), 1183–1199.
- Kotropoulos, C., Magnisalis, X., Pitas, I., Strintzis, M., 1994. Nonlinear ultrasonic image processing based on signal-adaptive filters and self-organizing neural networks. *IEEE Trans. Image Process.* 3 (1), 65–77.
- Lopata, R.G., Nillesen, M.M., Thijssen, J.M., Kapusta, L., de Korte, C.L., 2011. Three-dimensional cardiac strain imaging in healthy children using RF-data. *Ultrasound in Medicine & Biology* 37 (9), 1399–1408.
- Messas, E., Guerrero, J.L., Handschumacher, M.D., Chow, C.M., Sullivan, S., Schwammenthal, E., et al., oct 2001. Paradoxical decrease in ischemic mitral regurgitation with papillary muscle dysfunction: insights from three-dimensional and contrast echocardiography with strain rate measurement. *Circulation* 104 (16), 1952–1957.
- Moon, T., Nov 1996. The expectation-maximization algorithm. *Signal Process. Magazine, IEEE* 13 (6), 47–60.
- Myronenko, A., Song, X., Sahn, D., 2009. Maximum likelihood motion estimation in 3d echocardiography through non-rigid registration in spherical coordinates. In: Ayache, N., Delingette, H., Sermesant, M. (Eds.), *Functional Imaging and Modeling of the Heart*, vol. 5528. *Lecture Notes in Computer Science*. Springer, Berlin, Heidelberg, pp. 427–436.
- Nesser, H.-J., Mor-Avi, V., Gorissen, W., Weinert, L., Steringer-Mascherbauer, R., Niel, J., et al., 2009. Quantification of left ventricular volumes using three-dimensional echocardiographic speckle tracking: comparison with mri. *Eur. Heart J.* 30 (13), 1565–1573.
- Notomi, Y., Lysyansky, P., Setser, R.M., Shiota, T., Popović, Z.B., Martin-Miklović, M.G., et al., 2005. Measurement of ventricular torsion by two-dimensional ultrasound speckle tracking imaging. *J. Am. Coll. Cardiol.* 45 (12), 2034–2041.
- O'Donnell, M., Skovoroda, A.R., Shapo, B.M., Emelianov, S.Y.S., 1994. Internal displacement and strain imaging using ultrasonic speckle tracking. *IEEE Trans. Ultrason. Ferroelectr. Freq. Control* 41 (3), 314–325.
- Piboongunton, T., Aalo, V., Iskander, C.D., Efthymoglou, G., June 2005. Bivariate generalised Gamma distribution with arbitrary fading parameters. *Electron. Lett.* 41 (12), 709–710.
- Piella, G., Porras, A., De Craene, M., Duchateau, N., Frangi, A., et al., 2013. Temporal diffeomorphic free form deformation to quantify changes induced by left and right bundle branch block and pacing. In: Camara, O., Mansi, T., Pop, M., Rhode, K., Sermesant, M., Young, A. (Eds.), *Statistical Atlases and Computational Models of the Heart. Imaging and Modelling Challenges*, vol. 7746. *Lecture Notes in Computer Science*. Springer, Berlin, Heidelberg, pp. 134–141.
- Sherman, J., Morrison, W.J., 03 1950. Adjustment of an inverse matrix corresponding to a change in one element of a given matrix. *Ann. Math. Stat.* 21 (1), 124–127.
- Somphone, O., Dufour, C., Mory, B., Hilpert, L., Makram-Ebeid, S., Villain, N., et al., 2013. Motion estimation in 3D echocardiography using smooth field 744 registration. In: Camara, O., Mansi, T., Pop, M., Rhode, K., Sermesant, M., Young, A. (Eds.), *Statistical Atlases and Computational Models of the Heart. Imaging and Modelling 746 Challenges. Lecture Notes in Computer Science. Lecture Notes in Computer Science*. Springer, Berlin, Heidelberg, pp. 151–158.
- Stacy, E.W., 1962. A generalization of the Gamma distribution. *Ann. Math. Stat.* 1187–1192.
- Strintzis, M., Kokkinidis, I., june 1997. Maximum likelihood motion estimation in ultrasound image sequences. *IEEE Signal Process. Lett.* 4 (6), 156–157.
- Suffoletto, M.S., Dohi, K., Cannesson, M., Saba, S., Gorcsan, J., 2006. Novel speckle-tracking radial strain from routine black-and-white echocardiographic images to quantify dyssynchrony and predict response to cardiac resynchronization therapy. *Circulation* 113 (7), 960–968.
- Tautz, L., Hennemuth, A., Peitgen, H.-O., 2013. In: Camara, O., Mansi, T., Pop, M., Rhode, K., Sermesant, M., Young, A. (Eds.), *Statistical Atlases and Computational Models of the Heart. Imaging and Modelling Challenges*, vol. 7746. *Lect. Notes Comput. Sci.* Springer, Berlin, Heidelberg, pp. 169–177.
- Thirion, J.P., 1998. Image matching as a diffusion process: an analogy with maxwell's demons. *Med. Image Anal.* 2 (3), 243–260.
- Vegas-Sanchez-Ferrero, G., Aja-Fernandez, S., Palencia, C., Martin-Fernandez, M., 2012. A generalized gamma mixture model for ultrasonic tissue characterization. *Comput. Math. Methods Med.* 2012 (Article ID 481923), 1–25.
- Vegas-Sánchez-Ferrero, G., Martín-Martínez, D., Aja-Fernández, S., Palencia, C., 2010. On the influence of interpolation on probabilistic models for ultrasonic images. In: *Biomedical Imaging: From Nano to Macro, IEEE International Symposium on. IEEE Press*, pp. 292–295.
- Vercateren, T., Pennec, X., Perchant, A., Ayache, N., 2009. Diffeomorphic demons: efficient non-parametric image registration. *Neuroimage* 45 (1, Suppl. 1), S61–S72.
- Voigt, J.-U., Exner, B., Schmiedehausen, K., Huchzermeyer, C., Reulbach, U., Nixdorff, U., et al., 2003. *Circulation* 107 (16), 2120–2126.
- Yeon, S.B., Reichel, N., Tallant, B.A., Lima, J.A., Calhoun, L.P., Clark, N.R., 2001. Validation of in vivo myocardial strain measurement by magnetic resonance tagging with sonomicrometry. *J. Am. Coll. Cardiol.* 38 (2), 555–561.